NUMERICAL SIMULATION

OF FLUID-STRUCTURE INTERACTION PHENOMENA

Facoltà di Ingegneria

Dipartimento di Ingegneria Civile, Edile e Ambientale

Dottorato in Ingegneria Idraulica (XXXI ciclo)

Candidato: Luca Barsi

Matricola: 793557

Relatore: Giovanni Cannata

INDEX

Summary

In this thesis, a new method for the investigation of aeroelastic phenomena for long-span bridges is proposed: the aerodynamic fields and the motion of structure are simulated simultaneously and in a coupled manner. The structure is represented as a bidimensional elastically suspended rigid body with two degrees of freedom whose natural frequencies correspond to those of the fundamental flexural and torsional modes of vibration of the structure. The aerodynamic fields are simulated by numerically integrating the Unsteady Reynolds-Averaged Navier-Stokes (URANS) equations with a finite volume scheme on moving grids which adapt to the structural motion. The URANS equations are completed by the turbulent closure relations which are expressed as a function of the turbulent kinetic energy, the turbulence frequency and the strain tensor according to the k-ω SST approach. The presented model is used in order to identify the critical flutter wind velocity of the Forth Road Bridge deck, and the numerical results are compared with those of an experimental campaign. For wind velocities equal or greater than the critical wind flutter velocity, the deck starts to oscillate increasingly. It is demonstrated that the reason for the onset of the torsional-branch coupled flutter lies in the fact that, within each of the first oscillation cycles, there is a portion of the cycle in which the energy supplied by the aerodynamic field to the deck motion is more than the energy extracted in the rest of the cycle. Then it is shown that the reason for

the amplification of the instability resides in the drifting of large vortical formations along the deck surface. The numerical model is also used to test the effect, on the aeroelastic stability of the Forth Road Bridge deck, of the introduction of a couple of sloping barriers at the windward and leeward bridge deck edges. It is demonstrated that the aerodynamic modifications produced by the introduction of such barriers is effective in increasing the critical flutter velocity and mitigating the vibration amplitudes which develop during the flutter instability.

Chapter 1

Introduction

Long span bridges are susceptible to an oscillatory unstable aero-elastic phenomenon, named flutter, in which the bridge deck motion acquires a divergent character and the oscillation amplitudes grow rapidly to the point of causing the structural failure (Dowell, 2014). Bridge decks with bluff cross-sections are generally prone to the torsional flutter phenomenon: the case of the Tacoma Narrows Bridge deck is a well known example. Bridge decks with streamlined cross-sections are generally prone to the coupled (torsional-flexural) flutter phenomenon: the possibility that the latter kind of instability takes place is relevant in the case in which the bridge deck has torsional and flexural natural modes of oscillation closely spaced at low natural frequencies (Frandsen, 2004). Matsumoto et al. (2010) carried out analytical investigations on the mechanisms of coupled flutter. These authors distinguish two different types of coupled flutter. The first type is the torsional branch (TB) coupled flutter, which is dominated by a fundamentally torsional vibration and in which the vertical oscillations have small amplitudes. The second type is the heaving-branch (HB) coupled flutter, which is dominated by a fundamentally heaving vibration accompanied by torsional oscillations with small amplitudes.

Traditionally the critical flutter wind velocity of long span bridge decks is identified through the Scanlan approach (Nieto et al., 2014). A first central element of said approach lies in representing the structure as a bidimensional rigid body with two degrees of freedom, having mass per unit length and mass moment of inertia per unit length equal to those of the deck. In the above-mentioned schematisation the rigid body is considered as attached to an elastic vertical spring and to an elastic torsional spring whose stiffnesses are calibrated in order to give the natural frequencies corresponding to the fundamental flexural and torsional modes of vibration of the structure. Astiz (1998) highlights that schematising the structure as a bidimensional rigid body with two degrees of freedom supposes that there is full coherence between the shapes of the flexural and torsional modes of vibration along the span. The main criticism moved to the previous approach comes from Katsuchi et al. (1999). These authors underline that, in some cases, the possibility has been highlighted that in the coupled flutter not only the fundamental flexural and torsional modes of vibration participate in the instability: the latter authors notice that, in the coupled flutter, further modes of vibration can overlap the fundamental modes of vibration, giving rise to aeroelastic instability conditions characterized by more complex flutter mode shapes.

The original method proposed in this thesis is based on the need to overcome the limit of the Scanlan traditional approach, which substantially consists in using the above fundamental free modes of vibration and, starting from these modes, performing stability

analyses. Actually, also an elementary oscillator can oscillate not only with the fundamental vibration modes but also with other vibration modes, as a consequence of the load to which it is subjected. Consequently, a stability analysis which is able to overcome the above limitation must necessarily simulate the aerodynamic field and the structural motion in a coupled manner, given the fact that they interact each other.

A second central element of the above-mentioned Scanlan approach lies in modelling the aerodynamic forces as linear functions of the structural displacements, under the assumption of purely sinusoidal motions. This linear dependance is expressed via some appropriate coefficients, called *flutter derivatives*. The most widely used method for the evaluation of flutter derivatives is based on the following fundamental passages. The aerodynamic fields developing around a bridge deck cross-section (that is made to oscillate according to a predefined sinusoidal law of motion) are simulated. The time history of the forces produced by the aerodynamic fields on the bridge deck surface is approximated by a sinusoidal function. Consequently, the forces produced by the aerodynamic fields on the bridge deck are assumed to be linearly dependent on the structural displacements. From the above-mentioned linear dependence the flutter derivative calculation is performed.

Many authors (Larsen and Walther, 1998; Mendes and Branco, 1998; Taylor and Vezza, 2002; Morgenthal and McRobie, 2002; Vairo, 2003; Sarwar et al., 2008) propose models for the flutter derivatives estimation and use them in order to identify the critical flutter wind

velocity of the bridge decks.. Astiz (1998) and Dowell (2014) highlight that the linear relation between the forces produced by the aerodynamic field on the deck and the structural displacements (formulated in the Scanlan approach) proves to be acceptable only in the event that the amplitude of structural oscillations is limited. Furthermore, the same authors underline that the above-mentioned linear relation does not make it possible to take into account the effects of the unsteady vortical structures developed in the fluid-structure interaction. In this thesis (as said above), the aerodynamic fields and the motion of structure are simulated simultaneously and in a coupled manner. According to this approach, the pressure and velocity fluid fields, that develop around the structure at every instant, are simulated; starting from the aerodynamic pressures, the lift force and the twisting moment, acting on the structure at every instant, are computed; once the above-mentioned aerodynamic forces are known, the structural displacements are calculated; these displacements, in turn, modify the computational domain and the boundary for numerical integration of the fluid motion equations and, as a consequence, modify the structure of the aerodynamic fields. Thereby the limitation represented by the hypothesis of linear dependence of the aerodynamic forces from the structural displacements, which is a central element in the flutter derivatives approach, is exceeded. The simultaneous and coupled simulation of the aerodynamic fields and the structural motion allows the identification of the critical flutter wind velocity in a direct way. Furthermore, the approach based on the coupled and simultaneous simulation of

the aerodynamic fields and the structural motion proves to be more effective than that based on the flutter derivatives especially in cases where the fluid-structure interaction gives rise to the formation of large vortices which, produced at the leading edge, move towards the trailing edge and amplify the oscillations of the structure itself.

The latter methodology presents excessively high computational costs when applied to the three-dimensional simulation of the multimodal coupled flutter. However, Starossek (1998) underlines that schematizing the structure as a bidimensional system with two degrees of freedom makes it possible to favourably predict the critical flutter wind velocity when the modal shapes associated with the fundamental flexural and torsional modes of vibration do not greatly differ along the span-wise direction; in the latter case, the above-mentioned modes of vibration are able to couple and form a common flutter mode shape. In this context, as in the bimodal Scanlan approach, the structure can be represented as a bidimensional elastically suspended rigid body with two degrees of freedom whose natural frequencies correspond to those of the fundamental flexural and torsional modes of vibration of the structure. Braun and Awruch (2008) underline that the hypothesis of rigid body is acceptable when the elastic deformations of the deck cross-section can be considered small compared with the vertical and torsional displacements of the same deck cross-section.

The simulation of the aerodynamic fields can be performed by finite volume techniques on unstructured grids (Gallerano and Napoli, 1999; Oka and Ishihara, 2009) or on boundary-

conforming curvilinear grids (Gallerano and Cannata, 2011, Rossmanith et al., 2004). The continuity and momentum balance equations admit the velocity components and pressure as dependent variables. In the case of incompressible fluids, the pressure calculation can be performed by adopting explicit methods of fractional step type, or implicit methods of pressure-correction type. The first method is based on the calculation of a predictor velocity field from the momentum balance equation in which the term related to the pressure gradient is omitted: this field is not solenoidal but admits the same curl as that of the velocity field at the successive instant. A corrector irrotational field exists whose divergence is equal to those of the predictor field, but with opposite sign. This term is explicited in terms of a scalar function gradient. The laplacian of the scalar function equalized to the divergence (with negative sign) of the predictor velocity field allows the calculation of the above scalar function; from this function, the calculation of the corrector field can be performed and, consequently, also the calculation of the velocity field at the successive instant. The second method consists of gaining, from the velocity and pressure field at the instant t, the velocity and pressure field at the instant $t+\Delta t$ by means of the so-called outer iterations and inner iteration. A predictor velocity field is calculated at the outer iteration implicitly (by means of an inner iteration process), where the pressure gradient is assumed to be equal to that of the previous iteration. The predictor velocity field is introduced into the equation of the laplacian of the pressure, from the solution of which the pressure value is obtained. This pressure value

is in turn introduced in the momentum balance equation, thus providing the velocity field at the end of the *m-th* outer iteration. The outer iteration process ends when the velocity and pressure field at the instant $t+\Delta t$ satisfies both the continuity equation and the momentum balance equation.

.As said above, the instabilities of the decks are related to the unsteady phenomena of the aerodynamic fields (Larsen, 2000; Sarwar and Ishihara, 2010; Mannini et al., 2014), and in particular to the formation of unsteady vortex structures. In the literature, the most complete simulation of the turbulent flow fields is performed through the Large Eddy Simulation (LES) by applying a spatial filter to the fluid velocity fields and simulating all the vortex structures whose dimensions are equal or greater than those of the spatial filter. Bosch and Rodi (1998) highlight that at high Reynolds numbers, the stochastic turbulent fluctuations are superimposed on the periodic unsteady motion of the vortex structures. These authors proposed the simulation of the flow field characterized by the above-mentioned unsteady vortex structures by decomposing the instantaneous flow quantities in a time mean component, in a periodic component and in a turbulent fluctuating component. Following this approach, the sum of the time mean and the periodic part gives rise to the ensemble-averaged component of the flow quantities. The latter are calculated by the numerical integration of the ensemble-averaged continuity and momentum equations; the complete spectrum of the stochastic motion is simulated by a statistical turbulence model. The models coherent with the

above-mentioned approach are named in the literature as Unsteady Reynolds-Averaged Navier-Stokes (URANS) models. It must be highlighted that the URANS approach provides a more simplified representation of the aerodynamic field compared to the Large Eddy Simulation (LES) approach. On the other hand, the URANS methodology has relatively low computational costs. Furthermore, the URANS approach makes it possible (even though less rigorously than the LES approach) to simulate the quasi-periodic unsteady vortex structures of the aerodynamic field (Mannini et al., 2010) and (with reference to aeroelastic instability phenomena such as vortex induced vibrations and flutter) to well identify the onset velocities and the amplitudes of the induced structural oscillations.

The fluid velocity field around an object is always three-dimensional since (as has been said) is characterised by high vorticity, flow separation and unsteady vortex structures (Mannini et al., 2011). The bidimensional simulations are not able to adequately represent the energy transfer from the larger vortical structures to the smaller vortical structures, as this transfer is related to the vortex stretching (which is three-dimensional). However, Frandsen (2004) stresses that the effects of the aerodynamic field in the span-wise direction of the deck can be neglected in cases where the deck cross-section has sharp edges. Furthermore, many authors (Bruno and Khris, 2003; Mannini et al., 2010; Mannini et al., 2010b; Shimada and Ishihara, 2011) highlight that the aerodynamic field around the bridge decks show relevant quasi-periodic vortical structures characterised by the direction of the vorticity vector parallel

with the span-wise direction: the quasi-periodic vortical structures, characterised by the direction of the vorticity vector parallel to the transverse direction, are negligible in the opinion of the above-mentioned authors. In the above-mentioned conditions, bidimensional simulation schemes can produce acceptable results from an engineering point of view.

The above-mentioned authors follow the line indicated by Bosch and Rodi and simulate the aerodynamic instabilities by using a two-dimensional URANS model in which the fluid motion equations are completed by two turbulence statistical equation models. In the models proposed by the above-mentioned authors the span-wise diffusion processes are taken into account by a conveniently calibrated eddy viscosity introduced in the turbulent closure relations. The turbulent closure relations for the fluid motion equations are expressed as a function of the transport equations of turbulent kinetic energy k and the rate of viscous dissipation ε, or as a function of the transport equations of the turbulent kinetic energy and the turbulence frequency ω. Brusiani et al. (2013) argue that the k-ω model has to be preferred to the k-ε model for the simulation of the fluid dynamic fields near the wall: the k-ε model does not allow the direct integration through the boundary layer and over-estimates the turbulent kinetic energy in stagnation regions near the wall, while the k-ω model allows the direct integration through the boundary layer and improves the wall boundary layer unsteady solution, but is highly sensitive to the inlet turbulent boundary condition. Menter (2009)

proposed the k-ω Shear Stress Transport (SST) model, which consists of a blending between the k-ε model and k-ω model and preserves the main advantages of the k-ω model.

In this thesis, a new method for the investigation of aeroelastic phenomena for long-span bridges is proposed: the aerodynamic fields and the motion of structure are simulated simultaneously and in a coupled manner. The structure is represented as a bidimensional elastically suspended rigid body with two degrees of freedom whose natural frequencies correspond to those of the fundamental flexural and torsional modes of vibration of the structure. The Unsteady Reynolds Averaged Navier-Stokes (URANS) equations are solved on block-structured moving grids and are defined in integral form starting from the three-dimensional Leibniz rule and the substantial derivative of the material volume integral of the momentum. The solution procedure of the momentum balance equation in implicit form is of pressure-correction type. The finite-volume method of collocated type implies the reconstruction of the velocity and pressure values in the calculation cells which, in this thesis, uses the Rhie-Chow procedure.

The model has been validated by comparing the numerical results with the experimental ones related to a slender body with rectangular cross-section and the Forth-Road Bridge deck. The model validation is performed both in static conditions (i.e. under the assumption that all the degrees of freedom of the body are restrained) and dynamic conditions (i.e. under the

assumption that the body is free to oscillate in the bending degree of freedom and in the torsional degree of freedom). In the static case, the Strouhal number, the lift and drag coefficients are taken as benchmark parameters by comparing the numerical results with those obtained experimentally with regard to the case study of the slender body with rectangular cross-section. In the dynamic case, the comparison is performed in terms of critical flutter wind velocity by comparing the numerical results with those obtained experimentally with regard to the case study of the Forth Road Bridge deck.

A deep insight into the analysis and the detailed representation of the different phenomena that produce the onset of flutter for long span bridge decks with streamlined cross-section is proposed. Such detailed representation makes it possible to deduce that the reason for the coupled flutter onset lies in the fact that, within each of the first oscillation cycles, there is a portion of the cycle in which the energy supplied by the aerodynamic field to the deck motion is more than the energy extracted in the rest of the cycle. Moreover, the same detailed representation allows one to deduce that the reason for the amplification of the aeroelastic instability is ascribable to the formation and drift of large vortical formations along the surface of the deck. The numerical model is also used to test the effect, on the aeroelastic stability of the deck, of the introduction of a couple of sloping barriers at the windward and leeward bridge deck edges. It is demonstrated that the aerodynamic modifications, produced by the introduction of such barriers, is effective in increasing the

critical flutter velocity and mitigating the vibration amplitudes which develop during the

flutter instability.

Chapter 2

The model

In this chapter, the model utilized in order to perform the numerical investigation of the bridge flutter phenomenon is described. The chapter is organized as follows:

- in paragraph 2.1, the procedure is presented by which the integral form of the Navier-Stokes equations over a moving control volume is deduced;

- starting from the integral form of the Navier-Stokes equations over a moving control volume, in paragraph 2.2 the procedure is then presented by which the integral form of the Unsteady-Averaged Navier-Stokes (URANS) equations, which are numerically solved in this work, is deduced;

- in paragraph 2.3, the structural motion equations used in the present work are presented;

- in paragraph 2.4, a general overview on the implicit pressure correction methods is provided;

- in paragraph 2.5, the finite volume method is shown by which the URANS equations adopted in this work are solved.

2.1 Integral form of the Navier-Stokes equations over a moving control volume

In this paragraph, the Navier-Stokes equations are defined in integral form starting from the three-dimensional Leibniz rule and the substantial derivative of the material volume integral of the momentum.

Let ρ and $\vec{u}$ be, respectively, the density and the fluid velocity vector. Let $\Delta V_1(\tau)$ be a time-varying control volume bounded by a surface, of area $\Delta A_1(\tau)$, every point of which moves with a velocity that is different from the fluid velocity. By using the three dimensional Leibniz integral rule, the time derivative of the integral of $\rho\vec{u}$ over the volume $\Delta V_1(\tau)$ can be expressed as

$$\frac{d}{d\tau} \int_{\Delta V_1(\tau)} \rho\vec{u} \, dV_1 = \int_{\Delta V_1(\tau)} \frac{\partial \rho\vec{u}}{\partial \tau} dV_1 + \int_{\Delta A_1(\tau)} \rho\vec{u}(\vec{v} \cdot \vec{n}) \, dA_1 \qquad (1)$$

in which $\vec{n}$ is the outward unit vector normal to the surface of area $\Delta A_1(\tau)$ and $\vec{v}$ is the velocity vector with which the points belonging to the surface of area $\Delta A_1(\tau)$ move.

Let us consider a material fluid volume, i.e. a time-varying volume which moves with the fluid and always encloses the same fluid particles. Let $\Delta V(\tau)$ be a time-varying material volume and that is delimited by a surface of area $\Delta A(\tau)$ every point of which moves with the same velocity of the fluid. It is known that the time derivative of the integral of $\rho\vec{u}$ over the above material fluid volume (material derivative), $\frac{D}{D\tau} \int_{\Delta V(\tau)} \rho\vec{u} \, dV$, is expressed as (Aris, 1989)

$$\frac{D}{D\tau} \int_{\Delta V(\tau)} \rho \vec{u} dV = \int_{\Delta V(\tau)} \frac{\partial \rho \vec{u}}{\partial \tau} dV + \int_{\Delta A(\tau)} \rho \vec{u} (\vec{u} \cdot \vec{n}) \, dA \qquad (2)$$

in which the velocity vector with which the points belonging to the surface of area $\Delta A(\tau)$ coincides with the fluid velocity vector $\vec{u}$. It is assumed that at instant $\tau, \Delta V_1(\tau) = \Delta V(\tau)$. By replacing the first term on the right hand side of Eq. 2 by the term $\int_{\Delta V_1(\tau)} \frac{\partial \rho \vec{u}}{\partial \tau} dV_1$ extracted from the right hand side of Eq. 1, Eq. 2 becomes

$$\frac{D}{D\tau} \int_{\Delta V(\tau)} \rho \vec{u} dV = \frac{d}{d\tau} \int_{\Delta V_1(\tau)} \rho \vec{u} dV + \int_{\Delta A_1(\tau)} \rho \vec{u} (\vec{u} - \vec{v}) \cdot \vec{n} \, dA \qquad (3)$$

The left hand side of Eq. 3 represents the expression of the time derivative of the integral of $\rho \vec{u}$ over a material volume (material derivative), which is valid in the case of a control volume whose boundary surface points move with a velocity, $\vec{v}$, that is different from the fluid velocity, $\vec{u}$. By equating the rate of change of the momentum of a material volume, expressed by the right hand side of Eq. 3, to the total net force in this direction (Newton's law), we obtain the integral form of the momentum equation over a moving control volume

$$\frac{d}{d\tau} \int_{\Delta V_1(\tau)} \rho \vec{u} dV + \int_{\Delta A_1(\tau)} \rho \vec{u} (\vec{u} - \vec{v}) \cdot \vec{n} dA = \int_{\Delta V_1(\tau)} \rho \vec{f} dV + \int_{\Delta A_1(\tau)} \bar{T} \cdot \vec{n} dA \qquad (4)$$

in which $\bar{T}$ is the stress tensor. From Eq. 4, it is possible to deduce that, for an incompressible fluid, the integral form of the momentum equation over a moving control volume reads

$$\frac{d}{d\tau}\int_{\Delta V_1(\tau)}\vec{u}dV + \int_{\Delta A_1(\tau)}\vec{u}(\vec{u}-\vec{v})\cdot\vec{n}dA = \int_{\Delta V_1(\tau)}\vec{f}dV + \frac{1}{\rho}\int_{\Delta A_1(\tau)}\bar{T}\cdot\vec{n}dA \qquad (5)$$

in which

$$\bar{T} = -p\bar{I} + 2\mu\bar{S} \qquad (6)$$

where μ is the dynamic viscosity, $\bar{S}$ is the rate of strain tensor and $\bar{I}$ is the identity matrix. By introducing Eq. 6 into Eq. 5 and using the divergence theorem, Eq. 5 can be rewritten as

$$\frac{d}{d\tau}\int_{\Delta V_1(\tau)}\vec{u}dV + \int_{\Delta A_1(\tau)}\vec{u}(\vec{u}-\vec{v})\cdot\vec{n}dA = \int_{\Delta V_1(\tau)}\vec{f}dV - \frac{1}{\rho}\int_{\Delta V_1(\tau)}\nabla p dV$$

$$+ \int_{\Delta A_1(\tau)}2\nu\bar{S}\cdot\vec{n}dA \qquad (7)$$

in which ν is the dynamic fluid viscosity and $\nabla = \left(\frac{\partial}{\partial x} \quad \frac{\partial}{\partial y} \quad \frac{\partial}{\partial z}\right)$.

By adopting the same control volume, $\Delta V_1(\tau)$, the expression of the time derivative of the integral of ρ over the material fluid volume reads

$$\frac{D}{D\tau}\int_{\Delta V(\tau)}\rho dV = \frac{d}{d\tau}\int_{\Delta V_1(\tau)}\rho dV + \int_{\Delta A_1(\tau)}\rho(\vec{u}-\vec{v})\cdot\vec{n}dA \qquad (8)$$

From Eq. 8 it is possible to deduce that, for an incompressible fluid, the integral form of the continuity equation over a moving control volume reads

$$\frac{d}{d\tau}\int_{\Delta V_1(\tau)}dV + \int_{\Delta A_1(\tau)}(\vec{u}-\vec{v})\cdot\vec{n}dA = 0 \qquad (9)$$

Bearing in mind that $\Delta A(\tau)$ is the area of the surface delimiting the time-varying control

volume $\Delta V(\tau)$ that at instant τ coincides with the material volume, also the following relation

holds valid for an incompressible fluid

$$\int_{\Delta A(\tau)} \vec{u} \cdot \vec{n} dA = 0 \tag{10}$$

Following the same logical procedure already indicated for the definition of Eq. 3, if we

assume that, at instant τ, $\Delta V_1(\tau) = \Delta V(\tau)$ and introduce Eq. 10 into Eq. 9, we obtain

$$\frac{d}{d\tau} \int_{\Delta V_1(\tau)} dV + \int_{\Delta A_1(\tau)} \vec{v} \cdot \vec{n} \, dA = 0 \tag{11}$$

which is known in literature as the so-called Geometric Conservation Law (GCL, see

Hertel et al., 2013).

2.2 Integral form of the URANS equations over a moving control volume

Bosch and Rodi (1998) highlight that at high Reynolds numbers, the stochastic turbulent

fluctuations are superimposed on the periodic unsteady motion of the vortex structures. These

authors proposed the simulation of the flow field characterized by the above-mentioned

unsteady vortex structures by decomposing the instantaneous flow quantities in a time mean

component, in a periodic component and in a turbulent fluctuating component. Following this

approach, the sum of the time mean and the periodic part gives rise to the ensemble-averaged

component of the flow quantities. The latter are calculated by the numerical integration of the ensemble-averaged continuity and momentum equations; the complete spectrum of the stochastic motion is simulated by a statistical turbulence model. The models coherent with the above-mentioned approach are named in the literature as Unsteady Reynolds-Averaged Navier-Stokes (URANS) models.

Following this approach, the instantaneous values of the fluid velocity $\vec{u}(t)$ and the fluid pressure $p(t)$ are decomposed in the time mean components $\bar{\vec{u}}$ and $\bar{p}$, the periodic components $\tilde{\vec{u}}(t)$ and $\tilde{p}(t)$, and the fluctuating components $\vec{u}'$ and p'

$$\vec{u}(t) = \bar{\vec{u}} + \tilde{\vec{u}}(t) + \vec{u}' \tag{12}$$

$$p(t) = \bar{p} + \tilde{p}(t) + P' \tag{13}$$

The sum of the time mean and the periodic part are defined as the ensemble averaged component $\langle \vec{u}(t) \rangle$ and $\langle p(t) \rangle$, which are resolved in the numerical calculation. Eqs. (12), (13) become respectively

$$\vec{u}(t) = \langle \vec{u}(t) \rangle + \vec{u}' \tag{14}$$

$$p(t) = \langle p(t) \rangle + P' \tag{15}$$

For an incompressible fluid, by neglecting the viscous term the integral form of the ensemble averaged continuity and momentum equations over a moving control volume read

$$\frac{d}{d\tau} \int_{\Delta V_1(\tau)} dV + \int_{\Delta A_1(\tau)} (\langle \vec{u} \rangle - \vec{v}) \cdot \vec{n} dA = 0 \tag{16}$$

$$\frac{d}{d\tau} \int_{\Delta V_1(\tau)} \langle \vec{u} \rangle dV + \int_{\Delta A_1(\tau)} \langle \vec{u} \rangle (\langle \vec{u} \rangle - \vec{v}) \cdot \vec{n} dA = \int_{\Delta V_1(\tau)} \vec{f} dV - \frac{1}{\rho} \int_{\Delta V_1(\tau)} \nabla \langle p \rangle dV$$

$$+ \int_{\Delta A_1(\tau)} \bar{R} \cdot \vec{n} dA \tag{17}$$

in which $\bar{R}$ is the Reynolds stress tensor, which is defined as

$$\bar{R} = -\langle \vec{u}' \otimes \vec{u}' \rangle \tag{18}$$

where $\otimes$ is the tensor product operator. The unknown term $\langle \vec{u}' \otimes \vec{u}' \rangle$ is related to the ensemble averaged strain rate tensor $\langle \bar{S} \rangle$ and the ensemble averaged turbulent kinetic energy per unit mass $\langle k \rangle$ through the relation

$$\langle \vec{u}' \otimes \vec{u}' \rangle = -2\nu_t \langle \bar{S} \rangle + \frac{2}{3} \langle k \rangle \bar{I} \tag{19}$$

where ν_t is the kinematic eddy viscosity.

The turbulent closure relations for the fluid motion equations can be expressed as a function of the transport equations of turbulent kinetic energy k and the rate of viscous dissipation ε, or as a function of the transport equations of the turbulent kinetic energy and the turbulence frequency ω. Brusiani et al. (2013) argue that the k-ω model has to be preferred to the k-ε model for the simulation of the fluid dynamic fields near the wall: the k-ε model does not allow the direct integration through the boundary layer and over-estimates the turbulent

kinetic energy in stagnation regions near the wall, while the k-ω model allows the direct

integration through the boundary layer and improves the wall boundary layer unsteady

solution, but is highly sensitive to the inlet turbulent boundary condition. Menter (2009)

proposed the k-ω Shear Stress Transport (SST) model, which consists of a blending between

the k-ε model and k-ω model and preserves the main advantages of the k-ω model. In this

work, the turbulent closure relations are completed by the k-ω SST model. In integral form,

the integral form of the k and w equations over a moving control volume read

$$\frac{d}{d\tau} \int_{\Delta V_1(\tau)} \langle k \rangle dV + \int_{\Delta A_1(\tau)} \langle k \rangle (\langle \vec{u} \rangle - \vec{v}) \cdot \vec{n} dA = \int_{\Delta V_1(\tau)} \left[\frac{1}{\rho} \tilde{P}_k - \beta^* \langle k \rangle \langle \omega \rangle \right] dV$$

$$+ \int_{\Delta V_1(\tau)} \nabla \cdot [(\nu + \sigma_k \nu_t) \nabla \langle k \rangle] dV \tag{20}$$

$$\frac{d}{d\tau} \int_{\Delta V_1(\tau)} \langle \omega \rangle dV + \int_{\Delta A_1(\tau)} \langle \omega \rangle (\langle \vec{u} \rangle - \vec{v}) \cdot \vec{n} dA = \int_{\Delta V_1(\tau)} \left[\alpha \frac{1}{\rho \nu_t} \tilde{P}_k - \beta \langle \omega \rangle^2 \right] dV$$

$$+ \int_{\Delta V_1(\tau)} \nabla \cdot [(\nu + \sigma_\omega \nu_t) \nabla \langle \omega \rangle] dV + \int_{\Delta V_1(\tau)} \left[2(1 - F_1) \sigma_{w2} \frac{1}{\langle \omega \rangle} \nabla \langle k \rangle \cdot \nabla \langle \omega \rangle \right] dV \tag{21}$$

in which ‹ω› is the ensemble averaged turbulence frequency and

$$\nu_t = \frac{a_1 \langle k \rangle}{\max(a_1 \langle \omega \rangle, SF_2)} \tag{22}$$

$$S = \sqrt{2 \langle S_{ij} \rangle \langle S_{ij} \rangle} \tag{23}$$

$$\tilde{P}_k = \min(P_k, 10 \cdot \beta^* \rho \langle k \rangle \langle \omega \rangle) \tag{24}$$

$$P_k = \rho \nu_t \frac{\partial \langle u_i \rangle}{\partial x_j}\left(\frac{\partial \langle u_i \rangle}{\partial x_j} + \frac{\partial \langle u_j \rangle}{\partial x_i}\right) \tag{25}$$

$$F_1 = tanh\left\{\left\{min\left[max\left(\frac{\sqrt{\langle k \rangle}}{\beta^* \langle \omega \rangle y}, \frac{500\nu}{y^2 \langle \omega \rangle}\right), \frac{4\rho \sigma_{\omega 2} \langle k \rangle}{CD_{k\omega} y^2}\right]\right\}^4\right\} \tag{26}$$

$$F_2 = tanh\left[\left[max\left(\frac{2\sqrt{\langle k \rangle}}{\beta^* \langle \omega \rangle y}, \frac{500\nu}{y^2 \langle \omega \rangle}\right)\right]^2\right] \tag{27}$$

$$CD_{k\omega} = max\left(2\rho \sigma_{\omega 2} \frac{1}{\langle \omega \rangle}\frac{\partial \langle k \rangle}{\partial x_i}\frac{\partial \langle \omega \rangle}{\partial x_i}, 10^{-10}\right) \tag{28}$$

where *y* is the distance to the nearest wall, *S* is the invariant measure of the strain rate,

F_1 and F_2 are blending functions. All constants are computed as $\phi = \phi_1 F_1 + \phi_2 (1-F_1)$. The

constants for this model are: $\beta^* = 0.09$, $\alpha_1 = 5/9$, $\beta_1 = 3/40$, $\sigma_{k1} = 0.85$, $\sigma_{\omega 1} = 0.5$, $\alpha_2 = 0.44$,

$\beta_2 = 0.0828$, $\sigma_{k2} = 1$, $\sigma_{\omega 2} = 0.856$.

With respect to the turbulence modelling of the near-wall region, two different

approaches are usually adopted. The first one is the *Low-Reynolds Number* (LRN) approach,

which uses a refined mesh close to wall in order to resolve all the important physics. The

second one is the *High-Reynolds Number* (HRN) approach, which bridge the near-wall region

by using the wall functions. In this work, at the solid walls the near-wall treatment proposed

by Menter et al. (2003) is used. Such approach consists in automatically switching from a

LRN approach to a HRN approach as the grid is coarsened. The *k-ω* SST model has the

advantage that an analytical expression is known for *ω* in the viscous sub-layer and the

logarithmic region. However, the analytical expression of ω is not known in the buffer region. Therefore this method consists in blending the wall value of ω between the viscous sub layer and the logarithmic region. A blending function depending on y^+ is used ($y^+ = (y\, u_\tau)\, /\, \nu$ where y is the distance from the wall and u_τ is the friction velocity). The solutions for ω in the viscous sub layer and the logarithmic region are respectively

$$\omega_{Vis} = \frac{6\nu}{0.075\, y^2} \; ; \; \omega_{log} = \frac{1}{0.3\kappa}\frac{u_\tau}{y} \tag{29}$$

where κ is the Von Karman constant. They are reformulated in terms of y^+ and the following smooth blending is performed:

$$\omega_b(y^+) = \sqrt{\omega_{Vis}^2(y^+) + \omega_{log}^2(y^+)} \tag{30}$$

A similar formulation is used for the velocity profile near the wall

$$u_\tau^{Vis} = \frac{U_1}{y^+} \; ; \; u_\tau^{log} = \frac{U_1}{\frac{1}{\kappa}\ln(y^+) + C} \tag{31}$$

where U_1 is the velocity of the first calculation cell and

$$u_\tau = \sqrt[4]{(u_\tau^{Vis})^4 + (u_\tau^{log})^4} \tag{32}$$

This formulation gives the relation between the velocity near the wall and the wall shear stress. For the k-equation, a zero flux boundary is applied, as this is correct for both the low-Re and the logarithmic limit. The zero gradient boundary condition has been imposed at the

outlet for all the fluid dynamic quantities (fluid velocity, turbulent kinetic energy, turbulence frequency).

2.3 The structural motion equations

The motion of the body can be described in terms of three displacement components, ζ, η, θ, where ζ and η are respectively the translational displacement component in the horizontal direction x (positive from left to right) and the translational displacement component in the vertical direction y (positive upwards), and θ denotes the rotational displacement component (positive nose-up). The governing equation for the body motion is

$$M\,\ddot{X} + C\,\dot{X} + K\,X = F \tag{33}$$

where M, C and K are respectively the mass matrix, the damping matrix and the stiffness matrix; X is a vector which lists the displacement components ζ, η, θ; F is a vector which lists the component f_x in the x direction of the force exerted by the aerodynamic field on the body, the component f_y in the y direction of the above-mentioned force and the twisting moment m_θ generated by the above-mentioned force on the body. The components f_x, f_y and the twisting moment m_θ are calculated by integrating the pressures, the viscous stresses and the turbulent stresses over the surface of the structure.

By neglecting the displacements in the x-direction, Eq. (33) gives rise to two equations

$$m\ddot{\eta} + c_\eta\dot{\eta} + k_y\eta = f_y(\eta,\dot{\eta},\ddot{\eta},\theta,\dot{\theta},\ddot{\theta}) \qquad\qquad (34)$$

$$I\ddot{\theta} + c_\theta\dot{\theta} + k_\theta\theta = m_\theta(\eta,\dot{\eta},\ddot{\eta},\theta,\dot{\theta},\ddot{\theta}) \qquad\qquad (35)$$

where m and I are respectively the mass and the mass moment of inertia per unit length of the deck; c_y and c_θ are respectively the structural damping coefficients in the vertical and torsional degree of freedom; k_y and k_θ are respectively the stiffness constant of the vertical elastic spring and the stiffness constant of the torsional elastic spring, and η and θ are respectively the vertical displacement of the centre of gravity of the body and the rotational angle of the body around the shear centre. The stiffness k_y and k_θ are calibrated in order to give the natural frequencies corresponding to the fundamental flexural and torsional natural modes of vibration of the structure. The damping coefficients are calculated according to the formulation proposed in the work by Hines et al. (2009) on the basis of the given damping ratios.

2.4 Implicit pressure correction methods

The continuity and momentum balance equations admit the velocity components and pressure as dependent variables. In the case of incompressible fluids, the pressure calculation can be performed by adopting explicit methods of fractional step type, or implicit methods of pressure-correction type. The first method is based on the calculation of a predictor velocity

field from the momentum balance equation in which the term related to the pressure gradient is omitted: this field is not solenoidal but admits the same curl as that of the velocity field at the successive instant. A corrector irrotational field exists whose divergence is equal to those of the predictor field, but with opposite sign. This term is explicited in terms of a scalar function gradient. The laplacian of the scalar function equalized to the divergence (with negative sign) of the predictor velocity field allows the calculation of the above scalar function; from this function, the calculation of the corrector field can be performed and, consequently, also the calculation of the velocity field at the successive instant. The second method consists of gaining, from the velocity and pressure field at the instant t, the velocity and pressure field at the instant $t+\Delta t$ by means of the so-called outer iterations and inner iteration. A predictor velocity field is calculated at the outer iteration implicitly (by means of an inner iteration process), where the pressure gradient is assumed to be equal to that of the previous iteration. The predictor velocity field is introduced into the equation of the laplacian of the pressure, from the solution of which the pressure value is obtained. This pressure value is in turn introduced in the momentum balance equation, thus providing the velocity field at the end of the *m-th* outer iteration. The outer iteration process ends when the velocity and pressure field at the instant $t+\Delta t$ satisfies both the continuity equation and the momentum balance equation. Since in this work a solution procedure of pressure-correction type is

adopted for the solution of the momentum balance equation in implicit form, in the following a general overview on the implicit pressure correction methods is provided.

In general, if an implicit method is used to advance the fluid velocity in time, the discretized form of the momentum equation at the new time step $t + 1$ may be written as

$$a_P^{t+1}\vec{u}_P^{t+1} + \sum_N a_N^{t+1}\vec{u}_N^{t+1} = \vec{Q}^{t+1} - (\nabla p)_P^{t+1} \tag{36}$$

where P is the index of the arbitrary velocity node and N is the index of the generic neighbor node. Eq. 36 cannot be solved directly as the coefficients a (and possibly the source term $\vec{Q}$) depend on the unknown solution $\vec{u}^{t+1}$. It follows that Eq. 36 must be solved iteratively.

With regards to the simulation of an unsteady flow, two different levels of iterations exist within one time step. The first level refers to the so-called *outer iterations*, which are those iterations at the end of which the coefficients and the source term of the momentum equation are updated. The second level refers to the so-called *inner iterations*, which are those iterations that are performed on the momentum equation in which the coefficients and the source term are computed on the basis of the velocity and pressure field obtained at the previous outer iteration. On each outer iteration m, the following equation is solved by successive inner iterations

$$\tilde{a}_P^{m-1}\vec{u}_P^{m*} + \sum_N \tilde{a}_N^{m-1}\vec{u}_N^{m*} = \vec{Q}^{m-1} - (\nabla p)_P^{m-1} \tag{37}$$

in which the last term on the right hand side is computed on the basis of pressure field obtained at the end of the previous outer iteration. It is easy to deduce that the velocity field $\vec{u}^{m*}$ obtained by solving Eq. 37 does not normally satisfy the continuity equation. It follows that $\vec{u}^{m*}$ cannot represent the estimate of the solution $\vec{u}^{t+1}$ at the end of the current outer iteration; instead, it is a *predictor velocity field* (which is the reason for it carries an asterisk) and need to be corrected in order that the continuity equation is satisfied.

The predicted velocity value at node P, which has been obtained by solving Eq. 37, can be formally expressed by using the following relation

$$\vec{u}_P^{m*} = \frac{\vec{\tilde{H}}_P}{\tilde{a}_P^{m-1}} - \frac{1}{\tilde{a}_P^{m-1}} (\nabla p)_P^{m-1} \tag{38}$$

in which

$$\vec{\tilde{H}}_P = \vec{Q}_P^{m-1} - \sum_N \tilde{a}_N^{m-1} \vec{u}_N^{m*} \tag{39}$$

A better estimate of $\vec{u}^{t+1}$ at the end of the current iteration would be given by

$$\vec{u}_P^m = \frac{\vec{\tilde{H}}_P}{\tilde{a}_P^{m-1}} - \frac{1}{\tilde{a}_P^{m-1}} (\nabla p)_P^m \tag{40}$$

in which the pressure gradient $(\nabla p)_P^m$ is unknown. To follow, the procedure is shown by which the pressure gradient $(\nabla p)_P^m$ to introduce into Eq. 40 is calculated: bearing in mind that, for an incompressible flow, the discretized form of the continuity condition at the new time $t + 1$ may be written as

$$\sum_f \vec{u}_f \cdot \vec{n}_f^{t+1} A_f^{t+1} = 0 \tag{41}$$

we enforce the continuity condition by inserting the value of $\vec{u}_f^m$ into Eq. 41. According to the momentum interpolation method, if a collocated grid is used this velocity value can be expressed by mimicking Eq. 40 as follows

$$\vec{u}_f^m = \left(\frac{\vec{\tilde{H}}}{\tilde{a}}\right)_f - \left(\frac{1}{\tilde{a}}\right)_f (\nabla p)_f^m \tag{42}$$

where $\left(\frac{\vec{\tilde{H}}}{\tilde{a}}\right)_f$ and $\left(\frac{1}{\tilde{a}}\right)_f$ can be calculated by interpolating $\frac{\vec{\tilde{H}}_P}{\tilde{a}_P^{m-1}}$, $\frac{\vec{\tilde{H}}_N}{\tilde{a}_N^{m-1}}$ and $\frac{1}{\tilde{a}_P^{m-1}}$, $\frac{1}{\tilde{a}_N^{m-1}}$ respectively. By inserting Eq. 42 into Eq. 41, we obtain the so-called discretized Poisson pressure equation

$$\sum_f \left[\left(\frac{\vec{\tilde{H}}}{\tilde{a}}\right)_f\right] \cdot \vec{n}_f^{t+1} A_f^{t+1} = \sum_f \left[\left(\frac{1}{\tilde{a}}\right)_f (\nabla p)_f^m\right] \cdot \vec{n}_f^{t+1} A_f^{t+1} \tag{43}$$

Once Eq. 43 has been solved, the pressure gradient $(\nabla p)_P^m$ can be computed and used into Eq. 40 to correct the velocity value at node P. We then have, at the end of the current outer iteration, a velocity field which satisfies the continuity equation (and hence is called *corrector velocity field*), but both the velocity and pressure fields do not satisfy Eq. 36. We then begin another outer iteration, and the process is continued until a velocity field which satisfies both the momentum equation and the continuity equation is obtained.

Synthetically, with regards to the simulation of an unsteady incompressible flow on a collocated grid, the numerical procedure consists of the following passages:

1. based on the velocity field obtained at the previous outer iteration, calculate the coefficients $\tilde{a}_P^{m-1}$, $\tilde{a}_N^{m-1}$ and the source term $\vec{Q}^{m-1}$; furthermore, based on the pressure field obtained at the previous outer iteration, calculate the pressure term $(\nabla p)_P^{m-1}$;

2. solve Eq. 37 iteratively (inner iterations), thus obtaining $\vec{u}_P^{m*}$, $\vec{u}_N^{m*}$;

3. calculate $\vec{\tilde{H}}_P$, $\vec{\tilde{H}}_N$ from Eq. 39;

4. calculate $\left(\dfrac{\vec{\tilde{H}}}{\tilde{a}}\right)_f$ and $\left(\dfrac{1}{\tilde{a}}\right)_f$ by interpolating $\dfrac{\vec{\tilde{H}}_P}{\tilde{a}_P^{m-1}}$, $\dfrac{\vec{\tilde{H}}_N}{\tilde{a}_N^{m-1}}$ and $\dfrac{1}{\tilde{a}_P^{m-1}}$, $\dfrac{1}{\tilde{a}_N^{m-1}}$ respectively;

5. solve Eq. 43 iteratively (inner iterations), thus obtaining the pressure field at the current outer iteration m;

6. calculate $\vec{u}_P^m$, $\vec{u}_N^m$ from Eq. 40;

7. if the velocity field $\vec{u}^m$ satisfies the momentum equation, go to the next time step; otherwise, start another outer iteration and go to step 1.

2.5 The numerical model used in this work

In this paragraph, the finite volume method is shown by which Eqs. 10, 11 and 17 equations used in this work are solved. In order to make the text easier to follow, in the following the ensemble averaged quantities are not enclosed by brackets $\langle \ \ \rangle$.

2.5.1 Discretisation of the momentum equation

The discretised form of Eq. 17 is

$$\frac{3\vec{u}_P^{t+1}V_P^{t+1} - 4\vec{u}_P^t V_P^t + \vec{u}_P^{t-1}V_P^{t-1}}{2\Delta t} + \sum_f \left(\vec{n}_f^{t+1} \cdot \vec{u}_f^{t+1}A_f^{t+1} - \dot{V}_f^{t+1}\right)\vec{u}_f^{t+1}$$

$$= \sum_f \nu_{T,f}\,\vec{n}_f^{t+1} \cdot (\nabla\vec{u})_f^{t+1}S_f^{t+1} - (\nabla p)_p^{t+1}V_p^{t+1} \tag{44}$$

where the three-level second-order accurate backward scheme is used for temporal discretization (Ferziger and Peric, 2012). In Eq. 44, the subscript P and f indicate the cell-centre and the face-centre values of the generic fluid quantity, while $t+1$, t and $t-1$ indicate the new time instant and the two previous time instant.

The face-centre velocity $\vec{u}_f^{t+1}$ in the convective term of Eq. 44 is calculated by using the so-called Gamma interpolation scheme (Jasak et al., 1999). When this scheme reduces to a linear interpolation of the neighbouring cell-centre values, the face-centre velocity results by the relation

$$\vec{u}_f^{t+1} = f_x^{t+1}\vec{u}_P^{t+1} + (1 - f_x^{t+1})\vec{u}_N^{t+1} \tag{45}$$

in which $f_x = \dfrac{\overline{fN}}{\overline{pN}}$.

The face normal derivative of velocity $\vec{n}_f^{t+1} \cdot (\nabla\vec{u})_f^{t+1}$ in the diffusive term is calculated

as follows

$$\vec{n}_f^{t+1} \cdot (\nabla\vec{u})_f^{t+1} = \left|\vec{\Delta}_f^{t+1}\right|\frac{\vec{u}_N^{t+1} - \vec{u}_P^{t+1}}{\left|\vec{d}_{fn}^{t+1}\right|} + \left(\vec{n}_f^{t+1} - \vec{\Delta}_f^{t+1}\right) \cdot (\nabla\vec{u})_f^{t+1} \tag{46}$$

in which the second term at the right-hand side is used to take into account the non-

orthogonality of the mesh (Jasak, 1996).

By inserting Eqs. 45, 46 into Eq. 44, one obtains

$$\frac{3\vec{u}_P^{t+1}V_P^{t+1} - 4\vec{u}_P^t V_P^t + \vec{u}_P^{t-1}V_P^{t-1}}{2\Delta t} + \sum_f\left(\vec{n}_f^{t+1} \cdot \vec{u}_f^{t+1}S_f^{t+1} - \dot{V}_f^{t+1}\right)\left[f_x^{t+1}\vec{u}_P^{t+1} + (1 - f_x^{t+1})\vec{u}_N^{t+1}\right]$$

$$= \sum_f \nu_{T,f}\left[\left|\vec{\Delta}_f^{t+1}\right|\frac{\vec{u}_N^{t+1} - \vec{u}_P^{t+1}}{\left|\vec{d}_{fn}^{t+1}\right|} + \left(\vec{n}_f^{t+1} - \vec{\Delta}_f^{t+1}\right) \cdot (\nabla\vec{u})_f^{t+1}\right]A_f^{t+1} - (\nabla p)_p^{t+1}V_p^{t+1}$$

$$\tag{47}$$

By dividing Eq. 47 for V_P^{t+1} and by posing

$$a_P = \frac{1}{V_P^{t+1}}\left[\sum_f\left(\vec{n}_f^{t+1} \cdot \vec{u}_f^{t+1}A_f^{t+1} - \dot{V}_f^{t+1}\right)f_x^{t+1} + \nu_{T,f}\frac{\left|\vec{\Delta}_f^{t+1}\right|}{\left|\vec{d}_{fn}^{t+1}\right|}A_f^{t+1}\right] + \frac{3}{2\Delta t} \tag{48}$$

$$\vec{Q}_P^{t+1} = \frac{1}{V_P^{t+1}} \Sigma_f \left[\nu_{T,f} \left(\vec{n}_f^{t+1} - \vec{\Delta}_f^{t+1} \right) \cdot (\nabla \vec{u})_f^{t+1} A_f^{t+1} \right] + \frac{2V_P^t}{V_P^{t+1}\Delta t} \vec{u}_P^t - \frac{V_P^{n-1}}{2V_P^{t+1}\Delta t} \vec{u}_P^{t-1}$$

(49)

Eq. 47 can be rewritten as

$$a_P \vec{u}_P^{t+1} + \Sigma_N a_N \vec{u}_N^{t+1} = \vec{Q}_P^{t+1} - (\nabla p)_P^{t+1}$$

(50)

2.5.2 Derivation of the discretised pressure equation

The discretised form of Eq. 10 is

$$\Sigma_f \vec{n}_f^{t+1} \cdot \vec{u}_f^{t+1} A_f^{t+1} = 0$$

(51)

From Eq. 50 we have

$$\vec{u}_P^{t+1} = \frac{\vec{Q}_P^{t+1} - \Sigma_N A_N \vec{u}_N^{t+1}}{a_P} - \frac{1}{a_P} (\nabla p)_P^{t+1}$$

(52)

By posing

$$\vec{H}_P = \vec{Q}_P^{t+1} - \Sigma_N a_N \vec{u}_N^{t+1}$$

(53)

Eq. 52 can be rewritten as

$$\vec{u}_P^{t+1} = \frac{\vec{H}_P}{a_P} - \frac{1}{a_P} (\nabla p)_P^{t+1}$$

(54)

According to the momentum interpolation method (Norris, 2000), the cell-face velocity $\vec{u}_f^{t+1}$ in Eq. 51 can be expressed by mimicking Eq. 54 as follows

$$\vec{u}_f^{t+1} = \left(\frac{\vec{H}}{a}\right)_f - \left(\frac{1}{a}\right)_f (\nabla p)_f^{t+1} \tag{55}$$

where $\left(\frac{\vec{H}}{a}\right)_f$ and $\left(\frac{1}{a}\right)_f$ can be calculated by linearly interpolating $\frac{\vec{H}_P}{a_P}$, $\frac{\vec{H}_N}{a_N}$ and $\frac{1}{a_P}$, $\frac{1}{a_N}$ respectively (Rhie and Chow, 1983).

By inserting Eq. 55 into Eq. 51, the discrete pressure equation for the cell P is obtained

$$\sum_f \left(\frac{1}{a}\right)_f \vec{n}_f^{t+1} \cdot (\nabla p)_f^{t+1} A_f^{t+1} = \sum_f \vec{n}_f \cdot \left(\frac{\vec{H}}{a}\right)_f A_f^{t+1} \tag{56}$$

2.5.3 Calculation of the cell-face volume fluxes

The discretised form of Eq. 11 is

$$\frac{3V_P^{t+1} - 4V_P^t + V_P^{t-1}}{2\Delta t} - \sum_t \dot{V}_f^{t+1} = 0 \tag{57}$$

where the three-level second-order accurate backward scheme is used for temporal discretisation.

The difference between the cell volumes at consecutive time levels t, $t + 1$ can be calculated as

$$V_P^{n+1} - V_P^n = \sum_f \delta V_f^{t+1} \tag{58}$$

Analogously, the difference between the cell volumes at consecutive time levels $t - 1, t$ can be calculated as

$$V_P^n - V_P^{n-1} = \sum_f \delta V_f^t \tag{59}$$

It's easy to verify that, by simple passages, the following relations can be derived from Eqs. 58, 59

$$3V_P^{n+1} - 4V_P^n + V_P^{n-1} = \sum_f \left(3\delta V_f^{t+1} - \delta V_f^t \right) \tag{60}$$

By inserting Eq. 60 into Eq. 57, we obtain

$$\frac{1}{2\Delta t} \sum_f \left(3\delta V_f^{t+1} - \delta V_f^t \right) = \sum_f \dot{V}_f^{t+1} \tag{61}$$

from which it derives that, if the cell-face volume fluxes are calculated by means of the following expression

$$\dot{V}_f^{t+1} = \frac{3}{2} \frac{\delta V_f^{t+1}}{\Delta t} - \frac{1}{2} \frac{\delta V_f^t}{\Delta t} \tag{62}$$

Eq. 57 is identically satisfied.

2.5.4 Numerical calculation procedure

1. Calculate global lift force and twisting moment acting on the structure at the current time step.

2. Once the global face acting on the structure at the current time step are known, solve the equations governing the motion of the 2DOF system.

3. Once the displacements of the 2DOF system at the current time step are known, calculate the displacements of the mesh nodes belonging to the structure.

4. Together with the position of the boundary mesh nodes (which are fixed), the updated position of the mesh nodes belonging to the structure acts as a boundary condition for the mesh motion problem, whose solution provides the displacements of the interior mesh nodes. In this work, the mesh motion problem has been solved by using a mesh movement algorithm based on using Inverse Distance Weighting (see Uyttersprot, 2014).

5. Once the whole mesh is updated, calculate the cell-face volume fluxes using the expression

$$\dot{V}_f^{t+1} = \frac{3}{2}\frac{\delta V_f^{t+1}}{\Delta t} - \frac{1}{2}\frac{\delta V_f^t}{\Delta t} \tag{63}$$

6. Start the outer iteration loop in order to calculate the velocity and pressure filed at the current time step:

(i) solve the discretised momentum equation

$$\tilde{a}_P^{m-1}\vec{u}_P^{m*} + \sum_N \tilde{a}_N^{m-1}\vec{u}_N^{m*} = \vec{Q}^{m-1} - (\nabla p)_P^{m-1} \tag{64}$$

in which the coefficients a_P^{m-1}, $\tilde{a}_N^{m-1}$ and the source term $\vec{Q}^{m-1}$ are explicitly computed from the velocity field obtained at the end of the previous outer iteration and the cell-face volume fluxes obtained at step 6, and the pressure gradient $(\nabla p)_P^{m-1}$ is computed form the pressure field obtained at the end of the previous outer iteration;

(ii) solve the discretised pressure equation

$$\sum_f \left[\left(\frac{\vec{\tilde{H}}}{\tilde{a}} \right)_f \right] \cdot \vec{n}_f^{t+1} A_f^{t+1} = \sum_f \left[\left(\frac{1}{\tilde{a}} \right)_f (\nabla\rho)_f^m \right] \cdot \vec{n}_f^{t+1} A_f^{t+1} \tag{65}$$

in which the coefficients $\left(\frac{\vec{\tilde{H}}}{\tilde{a}} \right)_f$, $\left(\frac{1}{\tilde{a}} \right)_f$ are computed by linearly interpolating the corresponding coefficients $\frac{\vec{H}_P}{\tilde{a}_P}$, $\frac{\vec{H}_N}{\tilde{a}_N}$ and $\frac{1}{\tilde{A}_P}$, $\frac{1}{\tilde{A}_N}$ respectively, and the coefficients $\vec{H}_P$, $\vec{H}_N$ are computed from the velocity field obtained at step (i);

(iii) calculate the corrected velocity field by using the relation

$$\vec{u}_P^m = \frac{\vec{\tilde{H}}_P}{\tilde{a}_P^{m-1}} - \frac{1}{\tilde{a}_P^{m-1}} (\nabla p)_P^m \tag{66}$$

and update the cell-face values $\vec{n}_f^{t+1} \cdot \vec{u}_f^m S_f^{t+1}$ which appear in the convective term by using the relation

41

$$\vec{n}_f^{t+1} \cdot \vec{u}_f^m S_f^{t+1} = \left[\vec{n}_f^{n+1} \cdot \left(\frac{\vec{\vec{H}}}{\tilde{a}} \right)_f - \left(\frac{1}{\tilde{a}} \right)_f \vec{n}_f^{t+1} \cdot (\nabla p)_f^m \right] A_f^{t+1} \qquad (67)$$

in which the pressure gradient $(\nabla p)_f^m$ is computed from the pressure field obtained at

step (ii);

(iv) if the velocity field obtained at step (iii) satisfies the momentum equation, go to

step 1; otherwise, return to step (i).

Chapter 3

Test case 1: slender body with rectangular cross-section

In this chapter, the aerodynamic fields which develop around a slender body with rectangular cross-section with aspect ratio B/D equal to 5 (where B and D are respectively the width and the depth of the cross-section) are simulated. The static validation of the model (i.e. under the assumption that all the degrees of freedom of the cross-section are restrained) is performed by comparing numerical and experimental results. The simulations used for the static validation are performed for increasing Reynolds number values ($1.0 \times 10^3 < Re < 1.8 \times 10^5$). The model is also tested in dynamic conditions (i.e. the cross-section is free to oscillate in the bending degree of freedom and in the torsional degree of freedom). In Table 1 the values of the geometrical parameters (width and depth of the cross-section) and the structural parameters (bending vibration frequency and torsional vibration frequency of the body, bending and torsional damping ratios) adopted in the present numerical test are reported.

3.1. Geometry and numerical modelling

The flow domain considered for the body is 8B by 4B. The total number of cells is 36800. At the upwind boundary of the computational domain a zero gradient boundary

condition is imposed for the fluid pressure, while a constant value is set for the other fluid quantities (velocity, turbulent kinetic energy and turbulence frequency). For every simulation performed, the undisturbed wind velocity U set at the domain inlet derives from the Reynolds number used, the actual kinematic viscosity ($\nu = 1.23 \times 10^{-5}\ m^2/s$) and the width B of the cross-section. For the simulation performed at $Re = 5.0 \times 10^4$, at the solid walls the average value of the non-dimensional height y^+ is close to 3 and the maximum value is close to 6. The cell size varies gradually with a geometric progression ratio of 1.03 in all directions. At the solid walls the near-wall treatment proposed by Menter et al. (2003) is used. At the outlet a constant pressure boundary condition is set, while the zero gradient boundary condition is imposed for the other fluid dynamic quantities (fluid velocity, turbulent kinetic energy and turbulence frequency). In all the simulations performed to validate the model, a maximum Courant number of 1.0 is imposed.

3.2. Static validation

The time-averaged drag coefficient $C_D = F_D / (0.5\ \rho\ U^2\ D)$ and the time-averaged lift coefficient $C_L = F_L / (0.5\ \rho\ U^2\ B)$ (in which F_D and F_L are the drag and the lift forces exerted by the fluid on the structure, U the undisturbed wind velocity, D and B the depth and the width of the deck cross-section, ρ the fluid density) obtained numerically are reported in

Table 2 together with those evaluated in the wind tunnel tests performed by Schewe (2006, 2009). From Table 2 it can be seen that the values calculated from the numerical simulations are very close to those obtained experimentally by the latter author.

In Fig. 1 the Strouhal number values obtained numerically are reported together with those obtained in the wind tunnel test performed by Schewe (2013). For every simulation performed, the Strouhal number is calculated as $St = (f_s \ D) \ / \ U_\infty$, where the shedding frequency f_s is computed by the time history of the fluid velocity at the two different points placed in the wake of the body. From Fig. 1 it can be seen that the Strouhal number values calculated from the numerical simulations range between values of 0.11 and 0.12, in good agreement with the experimental data.

3.3. Dynamic simulations

The aerodynamic fields and the structural motion of the body in dynamic conditions (as previously defined) are simulated simultaneously and in a coupled manner for two different undisturbed wind velocity values. In Fig. 2 the time history of the torsional displacements obtained for a wind reduced velocity $U_\theta = 4.58$ ($U_\theta = U \ / \ (f_\theta B)$, where f_θ is the torsional vibration frequency of the body) is shown. In agreement with the results shown by Liu et al. (2012), for this wind reduced velocity the body exhibits the flutter behaviour. In particular,

coherently with that obtained numerically by the above authors, there is a phase in which the amplitude of the torsional displacements gradually increases, followed by a phase in which the amplitude of the same displacements reaches a nearly constant value. The simultaneous and coupled simulation of the aerodynamic fields and the structural motion is also performed for a wind reduced velocity $U_\theta = 3.05$. According to the experimental findings of the latter authors, from the numerical simulation it emerges that the amplitude of the oscillations of the body is substantially stable for this wind reduced velocity. In particular, in Fig. 3 the time history of the torsional displacements obtained from the simulation performed for this wind reduced velocity is shown: from Fig. 3, it can be seen that in this case the torsional displacements are very small.
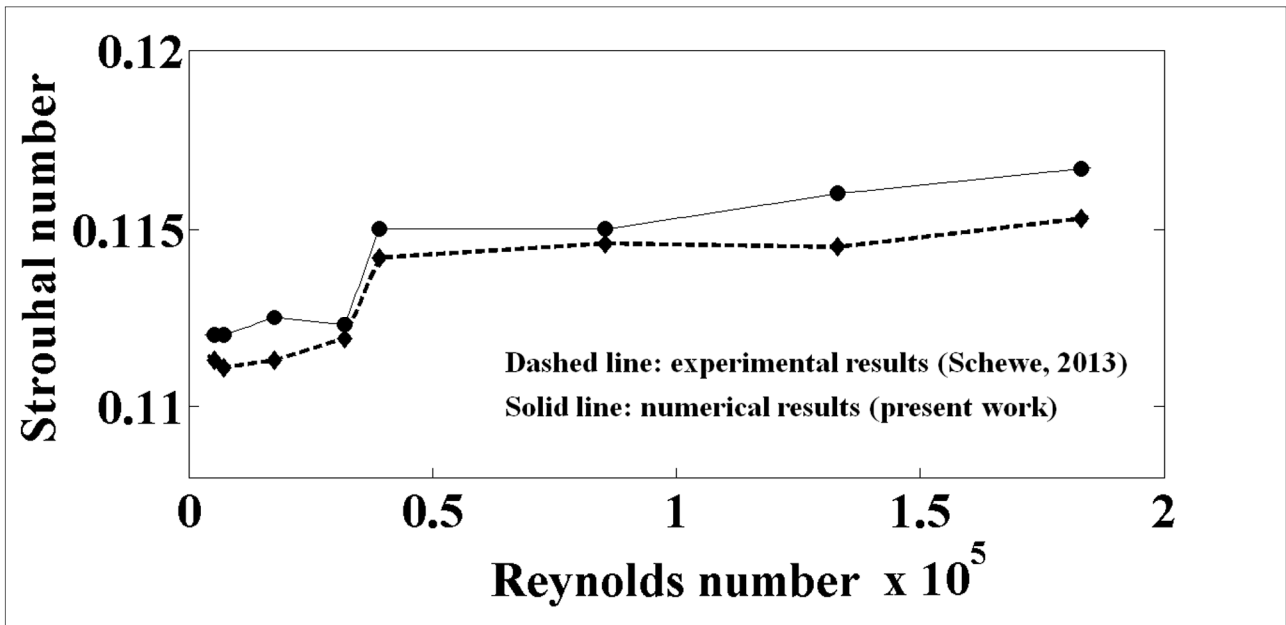
Figure 1. Strouhal number of the slender body with rectangular cross-section vs Reynolds number

Table 1. Geometrical and structural parameters of the slender body with rectangular cross-section	
Width	0.04 m
Maximum depth	0.008 m
Torsional damping ratio	0.50%
Heaving damping ratio	0.50%
Natural torsional frequency	180 Hz
Natural heaving frequency	120 Hz
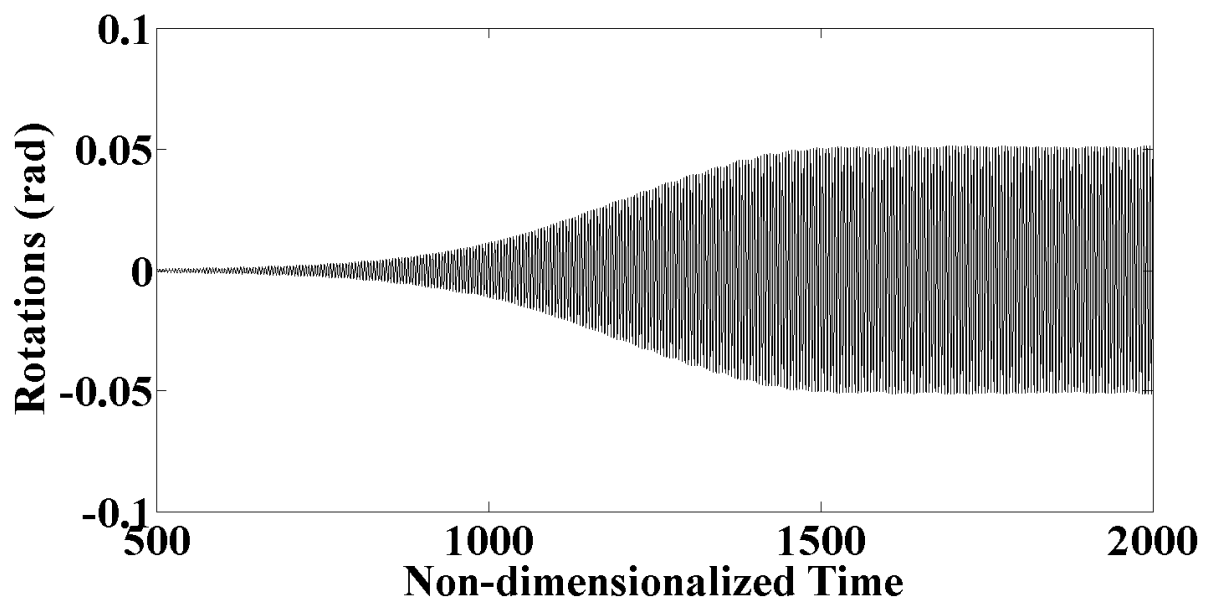
Figure 2. Time history of the torsional displacements of the slender body with rectangular cross-section

($U_\theta = 4.58$)
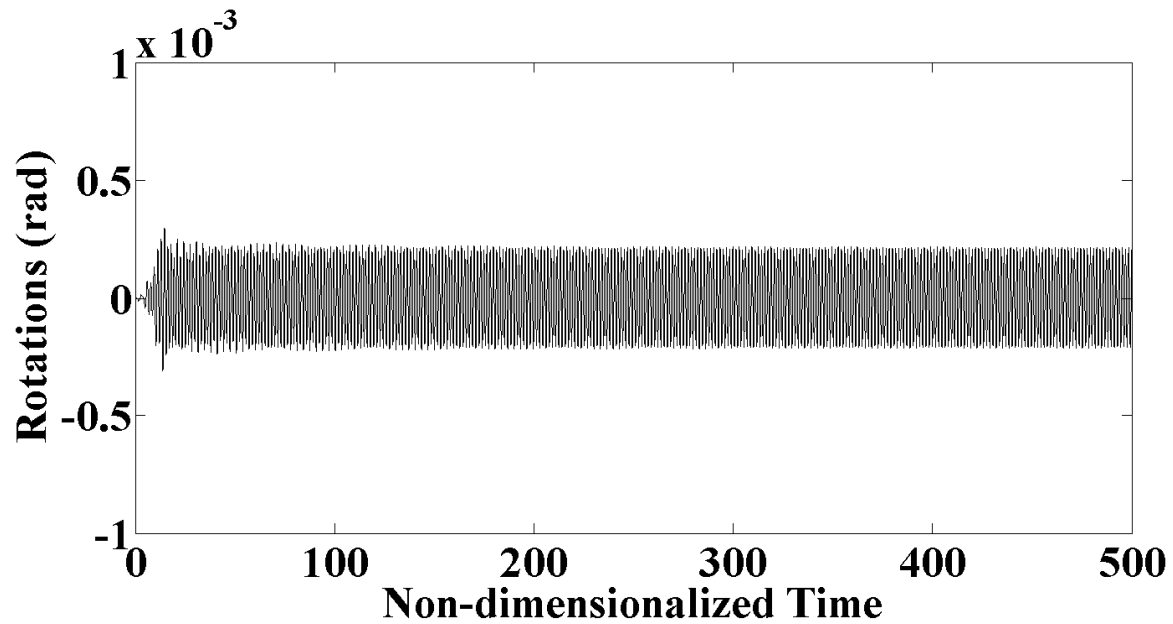
Figure 3. Time history of the torsional displacements of the slender body with rectangular cross-section

($U_\theta = 3.05$)

Chapter 4

Test case 2: Forth Road Bridge deck

In this chapter, the aerodynamic fields which develop around the Forth Road Bridge deck in its current configuration (Configuration I). In Fig. 4 the geometric characteristics of the Forth Road Bridge deck in the current configuration are shown. The dynamic validation of the model (i.e. under the assumption that the cross-section is free to oscillate in the bending degree of freedom and in the torsional degree of freedom) is performed by comparing numerical and experimental results.

The simulations used for the dynamic validation are performed for increasing Reynolds number values ($7.3 \times 10^3 < Re < 1.2 \times 10^4$). In Table 3 the values of the geometrical parameters (overall width and maximum depth) and the structural parameters (mass per unit length and mass moment of inertia per unit length, natural heaving frequency and natural torsional frequency, heaving and torsional damping ratios) of the Forth Road Bridge deck are listed. In order to perform the integration of the fluid motion equations near the wall without excessive computational costs, the simulations have been performed at a reduced scale (1:780).

4.1. Geometry and numerical modelling

The results related to the bridge deck in its current configuration are obtained by using a block-structured grid which is made up of 33850 cells. In this grid, a geometric progression of 1.02 for the cell size varying is used in all directions. The dimensions of the computational domain in the x and y directions are respectively equal to $Dx = 8B$ e $Dy = 4B$ (being B the width of the cross-section of the reduced-scale deck). For every simulation performed, the undisturbed wind velocity U set at the domain inlet derives from the Reynolds number used, the actual kinematic viscosity ($v = 1.23 \times 10^{-5}\ m^2/s$) and the width B of the reduced model cross-section. For the simulation performed at $Re = 1.0 \times 10^4$, at the solid walls the average value of the non-dimensional height y^+ is close to 4 and the maximum value is close to 11.

4.2. Initial conditions for the stability analysis

The initial conditions in the stability analyses must be treated carefully. The instantaneous application of the full wind speed to an initially stationary structure leads to large transient initial motions from which it is difficult to extract definitive conclusions about the stability of small oscillations. To eliminate this problem, (according to Frandsen, 2004) for every simulation the structural damping values are set close to the critical values for the first instants of the simulation until the structure settles into a near-stationary configuration,

after which the damping values are changed to their estimated values. During this transient phase, the stiffness constants of the vertical and torsional spring are gradually relaxed from magnified values to those calibrated to give the correct natural frequencies in the fundamental modes.

In Fig. 5 the time histories of the torsional displacements and the vertical displacements produced for a reduced wind velocity $U_\theta = 6.0$ are shown. From the figure it can be seen that, during the first instants of the simulation ($t < 0.08$) in which the structure is gradually released, the gravity centre slightly drifts downward from the equilibrium position and the deck slightly rotates in a clockwise direction. In the instants immediately after $t = 0.08$ the structure continues to rotate clockwise, so much so that the wind angle of attack exceeds the value for which the resultant of the aerodynamic forces and, consequently, the vertical displacement of the gravity centre change direction (from downward to upward). From the figure itself it can be seen that the oscillatory motion produced after this transient phase shows a slow but constant decay of both the vertical and angular displacements: the value of the imposed wind velocity ($U_\theta = 6.0$) lies under the critical flutter wind velocity value. In Fig. 6 the time histories of the rotations and the vertical displacements obtained for a reduced wind velocity $U_\theta = 7.0$ are shown. In both cases, a constant growth of the displacements is observed: the value of the imposed wind velocity ($U_\theta = 7.0$) lies above the critical flutter wind velocity. From Figs. 4(b), 5(b) it can be seen that the value of the mean rotation around which

the instantaneous values of the rotation oscillate is not fixed, but increases (in absolute value) going from the first to the second case. It follows that also the mean wind angle of attack increases (in absolute value) going from the first to the second case. Specifically, for $U_\theta = 6.0$ the instantaneous values of the wind angle of attack oscillate around a mean angle of attack roughly equal to -0.019 *rad*, whilst for $U_\theta = 7.0$ the instantaneous values of the wind angle of attack oscillate around -0.027 *rad*. Consequently the aerostatic vertical displacement, which is due to the aerostatic component of the wind load, increases from about 0.013 to about 0.05, i.e. more than linearly with the square of the wind velocity.

4.3 Dynamic validation

The model validation is performed by comparing the numerical results with those obtained from the wind tunnel tests described in Robertson et al. (2003). Fig. 7 shows the plot of the growth/decay rate of the rotations against the reduced velocity U_θ of the wind ($U_\theta = U / (f_\theta B)$, being f_θ the natural torsional frequency of the deck). From Fig. 7 it can observed that the reduced critical velocity obtained by the presented model is $U_\theta^* = 6.12$ (which corresponds to a full-scale critical wind velocity of 76.5 m/s). This value matches well the experimental result of $U_\theta^* \approx 6.35$ reported in Robertson et al. (2003). Furthermore, the frequencies of the rotational and the vertical motion of the deck are identified for the

considered reduced velocities U_θ. In agreement with that reported in Robertson et al. (2003),

it is found that at the point of flutter instability the frequencies of the translational and

rotational motion are identical.
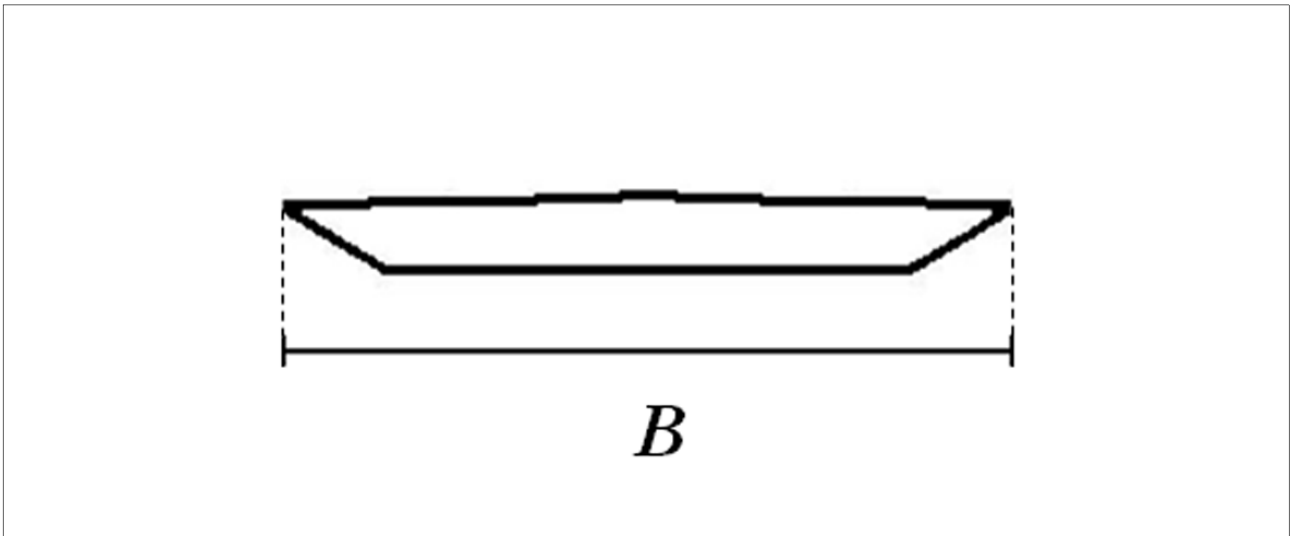
Figure 4. Forth Road Bridge deck cross-section in its construction state configuration

(Configuration I)

Table 3. Geometrical and structural parameters of the Forth Road Bridge deck (Robertson et al., 2003)	
Overall width	31.2 m
Maximum depth	3.2 m
Mass moment of inertia per unit length	2.13 x 10^6 kgm^2/m
Mass per unit length	17.3 x 10^3 kg/m
Torsional damping ratio	0.14%
Heaving damping ratio	0.31%
Natural torsional frequency	0.4 Hz
Natural heaving frequency	0.174 Hz

x 10^{-3}

(a)

(b)
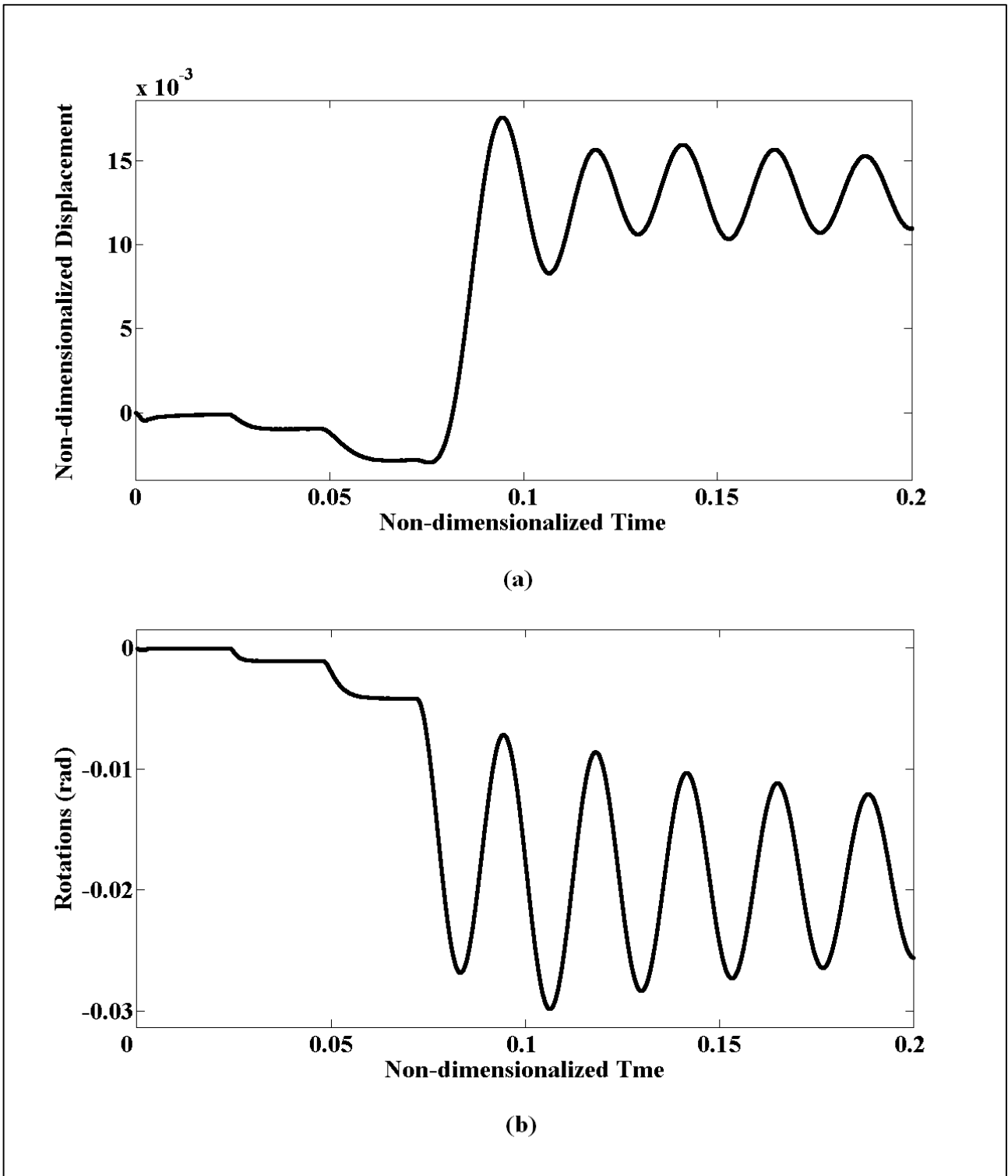
Figure 5. Time history of the vertical displacements (a) and the torsional displacements (b) of the Forth

Road Bridge deck (Configuration I - U_θ = 6.0)
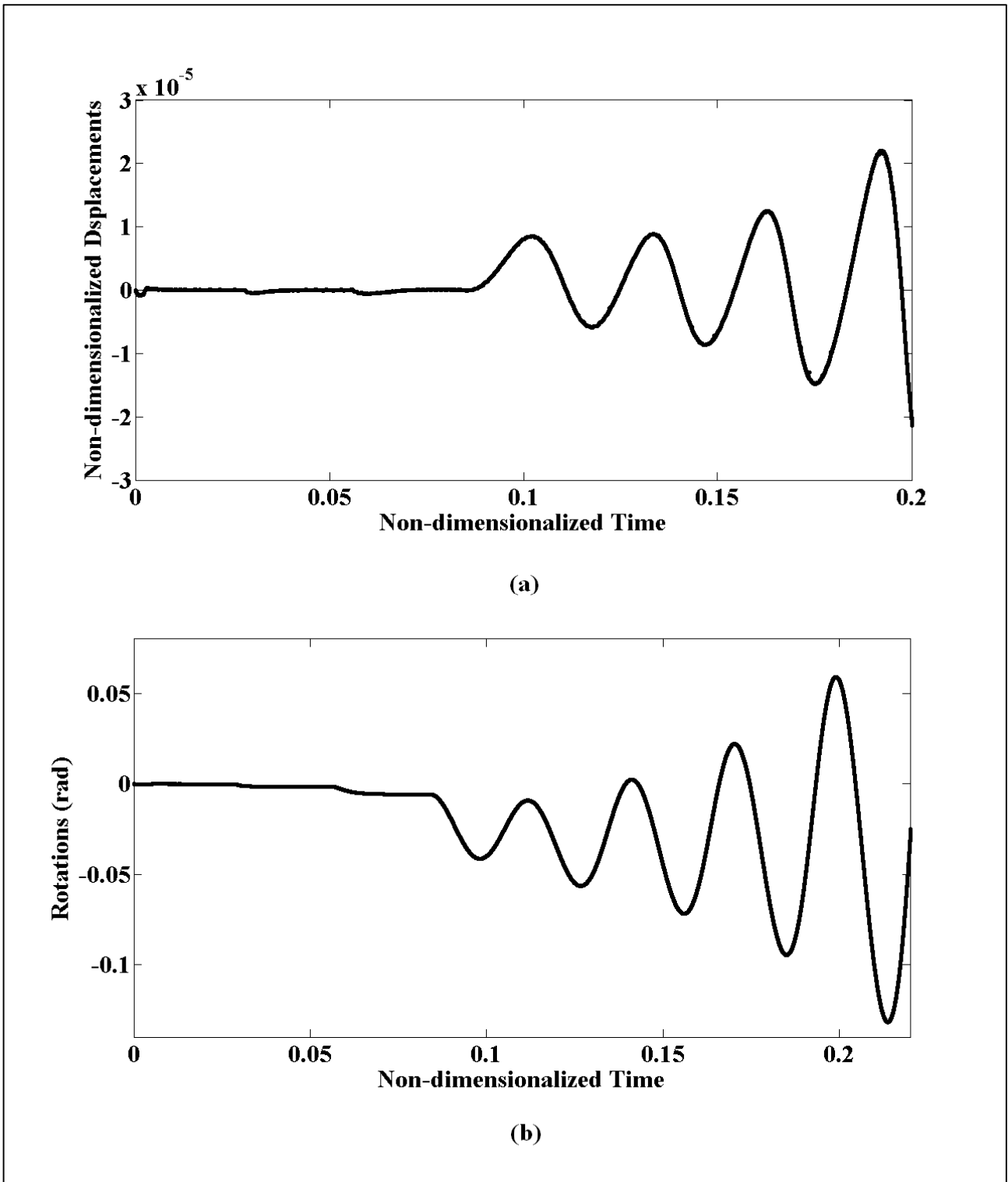
Figure 6. Time history of the vertical displacements (a) and the torsional displacements (b) of the Forth

Road Bridge deck (Configuration I - U_θ = 7.0)
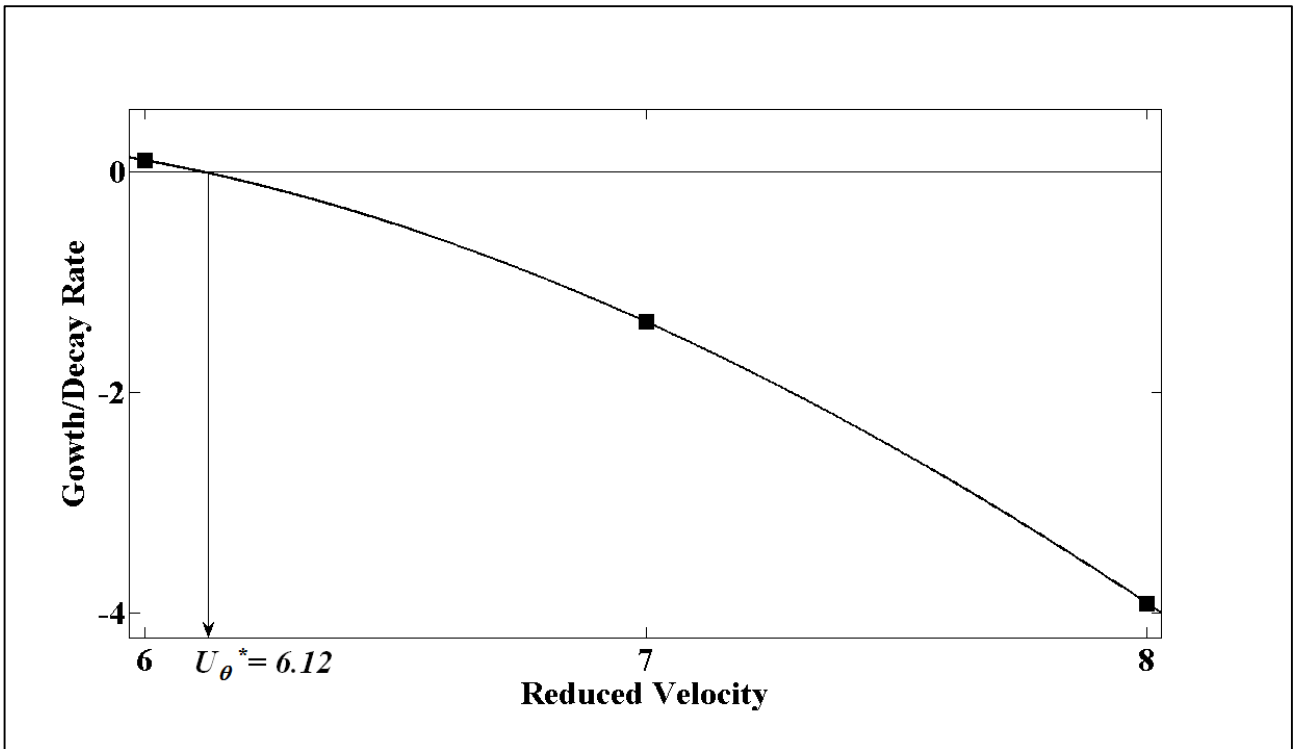
Figure 7. Growth/decay rate of the rotations of Forth Road Bridge deck vs reduced velocity

(Configuration I)

Chapter 5

Aeroelastic stability study of the Forth Road Bridge deck

In this section, the presented simulation model is utilised to analyse the full fluid-structure interaction of the Forth Road Bridge deck in the current configuration. A deep insight into the analysis and the detailed representation of the different phenomena that produce the onset of flutter for long span bridge decks with streamlined cross-section is proposed. In particular, at first it is identified the type of coupled flutter to which the Forth Road bridge deck is prone. It is then demonstrated that the reason for the onset of the torsional-branch coupled flutter lies in the fact that, within each of the first oscillation cycles, there is a portion of the cycle in which the energy supplied by the aerodynamic field to the deck motion is more than the energy extracted in the rest of the cycle. Lastly, it is shown that the reason for the amplification of the instability resides in the drifting of large vortical formations along the deck surface.

5.1 Coupled flutter type characterisation

In order to characterise the type of coupled flutter to which the Forth Road Bridge deck is prone, consistently with the treatise of Matsumoto et al. (2010) the angle Ψ defined as the

phase lag of the heaving response (vertical displacements) to the torsional response (rotations) of the structure is used. The latter authors highlight that the motion of a deck cross-section undergoing coupled flutter can be regarded as the superimposition of two fundamental oscillatory motions: the *torsional fundamental mode* and the *heaving fundamental mode*. The first one (torsional fundamental mode) is defined as a substantially torsional oscillatory motion around a certain point apart from the mid-chord point, accompanied by a vertical oscillatory motion of small entity. In the torsional fundamental mode, the phase angle Ψ is equal to 0° or 180° depending on whether the centre of rotation is placed upstream or downstream the mid-chord point of the deck cross-section (see Figs. 8(a), 8(c)). The second fundamental oscillatory motion (heaving fundamental mode) is defined as a substantially vertical oscillatory motion accompanied by a torsional oscillatory motion of small entity. In the heaving fundamental mode, the phase angle Ψ is equal to 90° or -90° depending on whether the sign of the small rotation of the upward moving cross-section is clockwise or anti-clockwise (see Figs. 8(b), 8(d)). That said, the relative contributions of the torsional fundamental mode and the heaving fundamental mode to the structural instability are respectively quantified as the absolute values of the cosine and the sine of the above angle Ψ. According to the treatise of the above authors, the torsional branch (TB) coupled flutter is defined as a coupled (torsional-flexural) flutter instability dominated by the fundamental torsional mode previously defined. In the case under examination (Forth Road Bridge in its

current configuration), the phase angle Ψ is found to be equal to around -16°, so that the relative contribution of the torsional fundamental mode to the instability of the structure is quantified as a value equal to $|\cos (-16°)| = 0.96$ and the relative contribution of the heaving fundamental mode in a value equal to $|\sin (-16°)| = 0.27$. Therefore it is concluded that in its current configuration the Forth Road Bridge deck is prone to a TB coupled flutter in which the torsional fundamental mode clearly dominates the heaving fundamental mode.

5.2 Coupled flutter onset mechanism

In the following the onset mechanism of the aeroelastic instability is shown. The evolution of the aerodynamic fields and the structural motion for a reduced wind velocity U_θ = 7.0 is analysed during a structural oscillation cycle in which the oscillation amplitudes are still limited. In Fig. 9(a) the time histories of the infinitesimal vertical displacement of the gravity centre and the resultant of the forces (per unit area) normal to the deck surface exerted by the fluid on the structure (aerodynamic forces) are shown jointly. In Fig. 9(b) the time histories of the infinitesimal angular displacement of the deck and the twisting moment generated by the same resultant are shown jointly. The cycle of structural oscillation shown in Figs. 9(a), 9(b) corresponds to the time interval between two instants (indicated with the

letters A and E in Figs. 9(a), 9(b)) when the infinitesimal vertical displacement of the downward moving gravity centre assumes a relative minimum value.

- By observing Fig. 9(a) it is deduced that in the time interval between instants A and B the gravity centre moves downward and passes from the position which corresponds to the static equilibrium to the position of minimum height (within the considered cycle), when the vertical velocity of the gravity centre of the structure vanishes. In this interval the resultant of the aerodynamic forces is directed upward, thus acting in opposition to the downward translational motion of the deck and, consequently, provides a damping effect on the same translational motion.

- In the time interval between instants B and C the gravity centre of the structure inverts the direction of the translational motion and passes from the position of minimum height to the position which corresponds to the static equilibrium, when the vertical velocity of the gravity centre assumes a relative maximum value. In this interval the resultant of the aerodynamic forces, which is still directed upward, acts in the same direction as that of the upward translational motion of the deck and then produces an effect of amplification of the same motion.

- In the time interval between instants C and D the gravity centre of the deck still moves upward until it reaches the position of maximum height (within the considered oscillation cycle), when the vertical velocity of the gravity centre vanishes again. In this

interval the magnitude of the resultant of the aerodynamic forces switches from positive values to values close to zero. Within this interval the above resultant acts in the same direction as that of the upward translational motion of the deck and then still amplifies the translational motion of the deck.

- In the time interval between the instants D and E the gravity centre of the structure inverts the direction of the translational motion and passes from the position of maximum height to the position which corresponds to the static equilibrium, when the vertical velocity of the gravity centre assumes a relative minimum value. In this last portion of the oscillation cycle the resultant of the aerodynamic forces starts to grow one more from values close to zero. In this interval the above resultant acts in opposition to the downward translational motion of the deck and then provides a damping effect of the same translational motion.

The examination of Fig. 9 stresses that during the time interval A-B and D-E of the above cycle the resultant of the aerodynamic forces acts in the opposite direction to the vertical velocity of the deck gravity centre, whilst in the time interval B-D the resultant acts in the same direction as the vertical velocity. The result of the integral of the work, defined as the product between the resultant and the infinitesimal displacement of the gravity centre of the deck, over the interval B-D is approximately equal to 9.63×10^{-5} J. This integral is much higher, in absolute value, than the sum of the integral calculated over A-B (approximately -3.51×10^{-5} J) and the integral calculated over D-E (approximately -1.95×10^{-5} J). The net

energy contribution (approximately 4.17×10^{-5} J) of the resultant of the aerodynamic forces to the translational motion of the deck is that of making the same motion unstable.

Similar considerations can be made regarding the twisting moment generated by the resultant of the aerodynamic forces. As shown in Fig. 9(b), in the time intervals between the instants A and B1 and the instants D1 and E the deck rotates clockwise and the above moment acts in the same direction as that of the angular velocity. In these intervals the twisting moment provides an effect of amplification of the rotating motion. In the time interval between the instants B1 and D1 the deck rotates counter-clockwise and the above moment acts in the opposite direction as that of the angular velocity. In this interval the twisting moment provides a damping effect of the rotational motion of the deck. The result of the integral of the work, defined as the product between the twisting moment and the infinitesimal rotation of the deck, over the whole oscillation cycle A-E is approximately equal to 0.15×10^{-5} J. Then it is deduced that the net energy contribution provided from the twisting moment to the rotational motion has a destabilising effect on the same rotational motion.

Based on the analysis of the aerodynamic fields and the structural motion during the first cycles of oscillations of the deck (when the structure still exhibits oscillations of small amplitudes), it is then possible to deduce that the reason for the onset of the instability lies in the fact that there are some portions of the cycle, within each of the first oscillation cycles, in

which the aerodynamic field provides both the translational and the rotational motion with a higher supply of energy than that subtracted from the deck motion in the rest of the cycle.

Once the two-degree-of-freedom instability has been triggered, a progressive increase of the maximum amplitudes of the rotation angle takes place. As shown in the following subsection, once a threshold value of the above angle is exceeded the recirculation bubble, which pulsates in proximity of the leading edge during the onset phase just described, starts to drift along the deck surface. From this point on, the modalities of amplification of the oscillations have a different dynamic to the one described above.

5.3 Post-critical flutter mechanism

In the following the mechanism of amplification of the aeroelastic instability is shown in detail. The evolution of the structural motion and the aerodynamic fields which develop for a reduced wind velocity $U_\theta = 7.0$ within ½ cycle of oscillations of the structure, in which the amplitudes of the oscillations have reached high values, is shown. Figs. 10(a), 10(c), 10(e), 10(g) show the fluid velocity fields that develop around the deck in four instants within this ½ cycle. By ½ cycle of structural oscillations is meant the temporal interval between the instant when the gravity centre of the downward moving structure corresponds to the static equilibrium position of the structure's centre of gravity and the instant when the gravity centre

of the upward moving structure corresponds to the static equilibrium position of the structure's centre of gravity. In Figs. 10(b), 10(d), 10 (f), 10 (h) are shown the distributions of the forces per unit area normal to the deck surface exerted by the fluid on the structure (aerodynamic forces) in the same instants.

- In the first of the four considered instants a downward translation and a clockwise rotation of the deck is ongoing. The angle of attack is sufficiently high to cause the flow detachment near the leading edge. In Fig. 10(a) the vortex formed immediately downline this detachment zone is shown. In Fig. 10(b) the distribution of the aerodynamic forces can be seen. The resultant of these forces is an upward force directed normally to the upper surface of the deck. In this instant, this resultant acts in opposition to the downward velocity of the gravity centre and, therefore, provides a damping effect on the translational vertical motion of the deck. The point of application of the resultant is placed near the centre of the vortex, in an extremely far position from the mid-chord point of the deck cross-section. This resultant gives rise to a clockwise twisting moment which prevails against the elastic and the damping moment acting in the same instant and, together with the inertial torque, leads to an amplification of the clockwise rotation of the deck.

- In Fig. 10(c) it can be seen that, compared to the previous instant, the vortex has drifted along the upper surface toward the trailing edge. This change of position is accompanied with a growth in the dimensions of the vortical formation. By observing Fig.

10(d) it can be seen that an overall increase of the aerodynamic forces is associated to the growth of the vortex. The point of application of the resultant, placed near the centre of the vortex, has got close to the mid-chord point of the deck cross-section. The effect produced by the increase of the intensity of the resultant prevails against the effect produced by the change of its point of application, causing an increase of the intensity of the clockwise twisting moment due to this resultant. Consequently this twisting moment acts in opposition to the elastic and the damping moment and, together with the inertial torque, produces a further amplification of the clockwise rotation of the deck. As well as in the previous instant, the resultant of the aerodynamic forces acts in opposition to the downward translational motion of the gravity centre and, therefore, still provides a damping effect on the motion itself.

- By examining Fig. 10(e) it can be seen that, compared to the previous instant, the vortex has further drifted along the upper surface, getting close to the trailing edge. In Fig. 10(f) it is seen that an overall increase of the aerodynamic forces corresponds to the growth of the vortex. At the same time it can be seen that the point of application of the resultant has got closer to the mid-chord point of the deck cross-section. The effect produced by the change of position of the resultant's point of application prevails against the effect produced by the increase of its intensity, causing a decrease of the intensity of the clockwise twisting moment due to this resultant. The twisting moment continues to act in opposition to the elastic and the damping moment, but its intensity has reduced.

- In the latest of the four considered instants the inversion of the translational and rotational motion of the deck has taken place. In Fig. 10(g) it is shown that the vortex still drifts along the upper surface till reaching the trailing edge. Fig. 10(h) shows the distribution of the aerodynamic forces. The resultant of these forces slightly decreases compared to the previous instant. The point of application of the resultant, previously placed between the leading edge and the mid-chord point, is now placed between the mid-chord point and the trailing edge. Consequently the moment due to the resultant changes sign and, as a result of the simultaneous change in the rotation direction of the deck, acts in the same direction as that of the angular velocity. In this instant, the resultant of the aerodynamic forces acts in the same direction as the upward velocity of the gravity centre. Consequently, in such instant the above resultant provides a contribution in the amplification of the upward translational motion of the deck.

From the examination of Figs. 10(a), 10(c), 10(e), 10(g) and 10(b), 10(d), 10(f), 10(h) it results that the reason for the amplification of the instability lies in the formation and the drift of large vortical formations along the deck surface. From the simulation of the phenomenon it emerges that, during the whole ½ cycle of structural oscillations (as previously defined), the sign of the twisting moment generated by the resultant of the components normal to the upper surface of the forces acting on the structure is always coherent with the sign of rotation. Consequently, there is a continuous supply of energy from the fluid dynamic field to the

structure, that constitutes the reason for the amplification of the instability of the torsional motion. The result of the integral of the work, defined as the product between the resultant and the infinitesimal displacement of the gravity centre of the deck, over the whole cycle of structural oscillation is positive. Consequently, the net effect of the resultant on the translational motion of the deck is to amplify the above-mentioned motion and provide a destabilising contribution.

Figure 8. Fundamental oscillatory motions in coupled flutter: (a) torsional fundamental

mode with Ψ=0°, (b) heaving fundamental mode with Ψ =-90°, (c) torsional fundamental mode

with Ψ =180°, (d) heaving fundamental mode with Ψ =90°
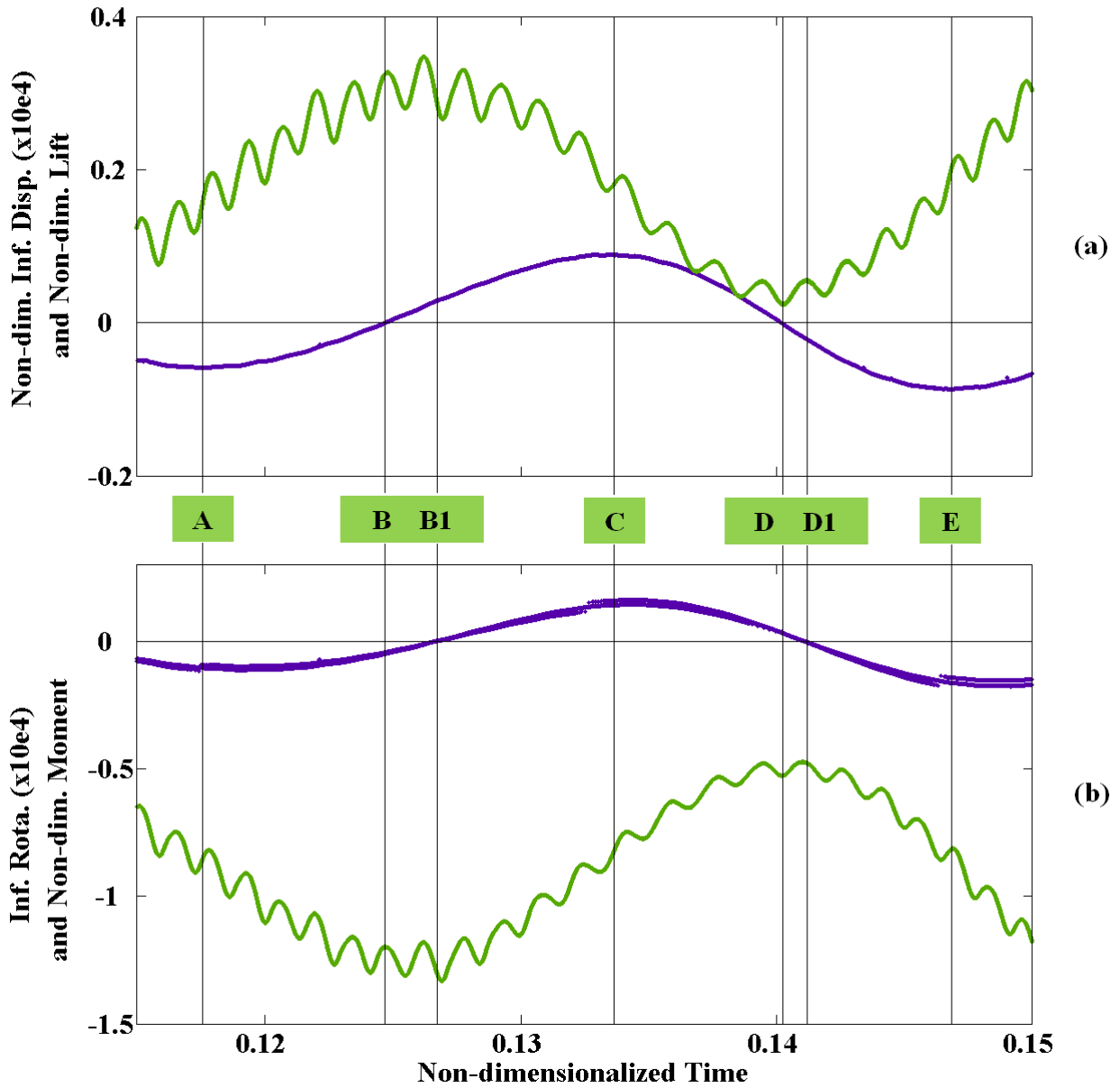
Figure 9. (a) Time histories of the infinitesimal vertical displacement of the gravity centre (blue) and the

resultant of the aerodynamic forces (green); (b) time histories of the infinitesimal angular displacement of

the deck (blue) and the twisting moment generated by the resultant (green)

70
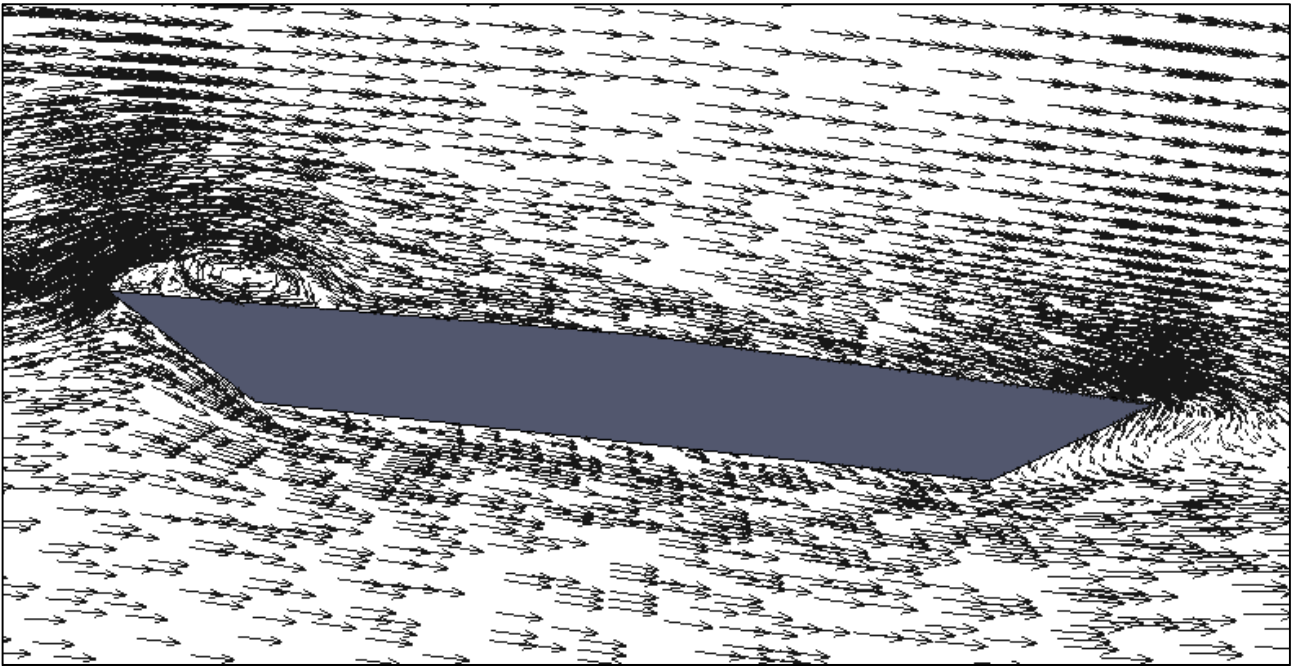
Figure 10(a). Forth Road Bridge deck (Configuration I): velocity fields of the fluid at T1
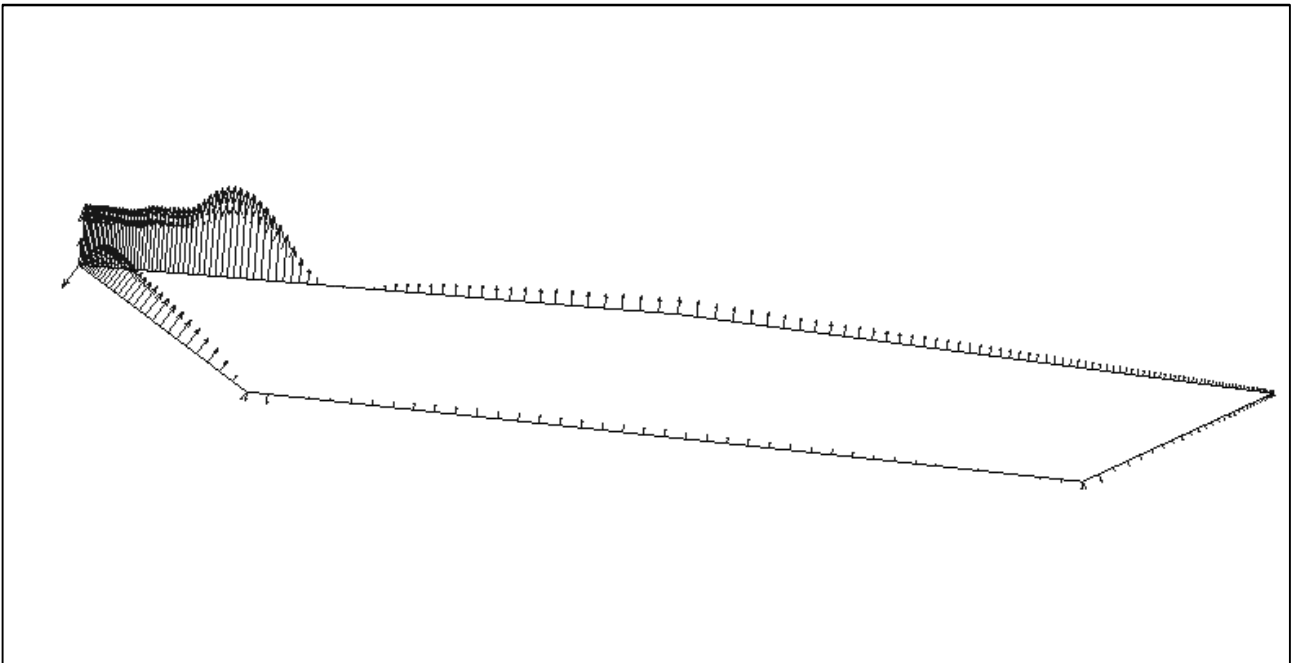
Figure 10(b). Forth Road Bridge deck (Configuration I): surface pressures at T1
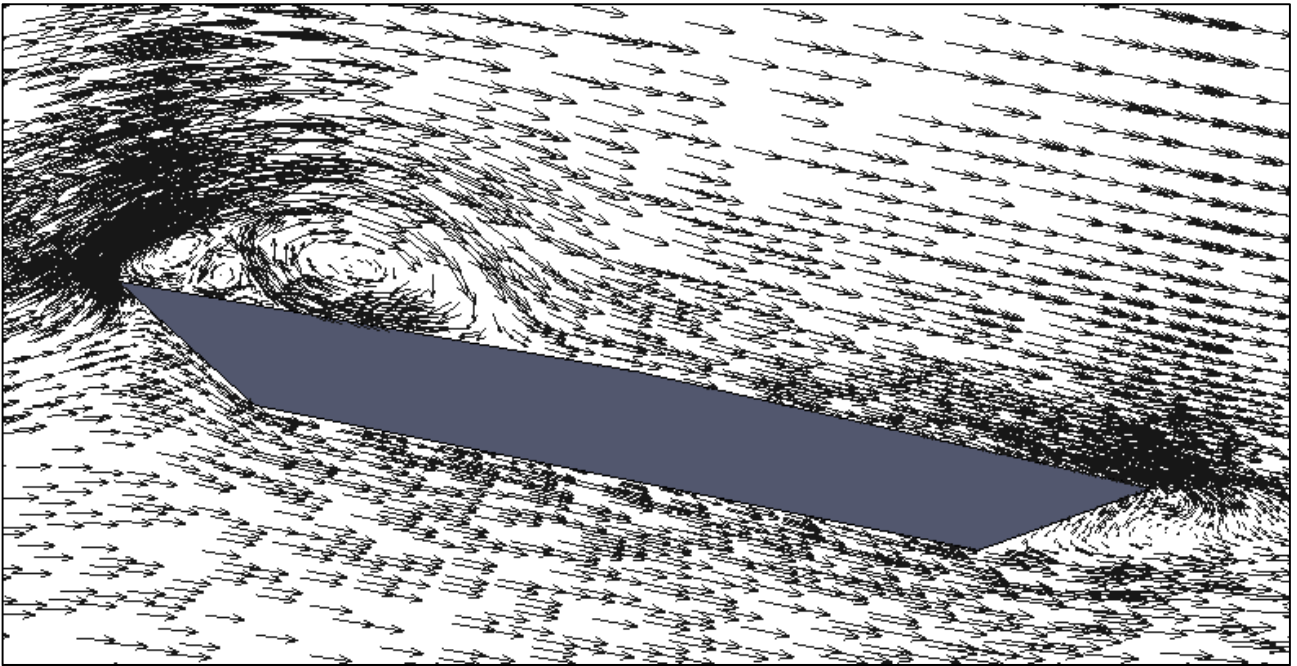
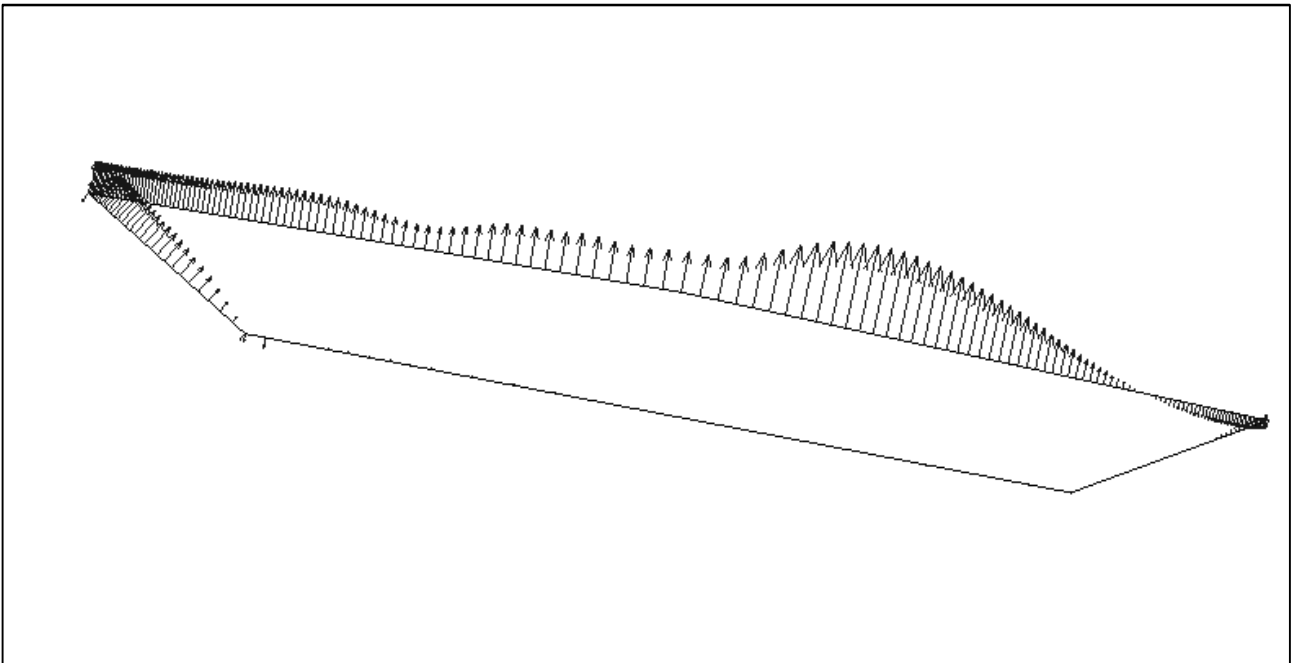Figure 10(c). Forth Road Bridge deck (Configuration I): velocity fields of the fluid at T2
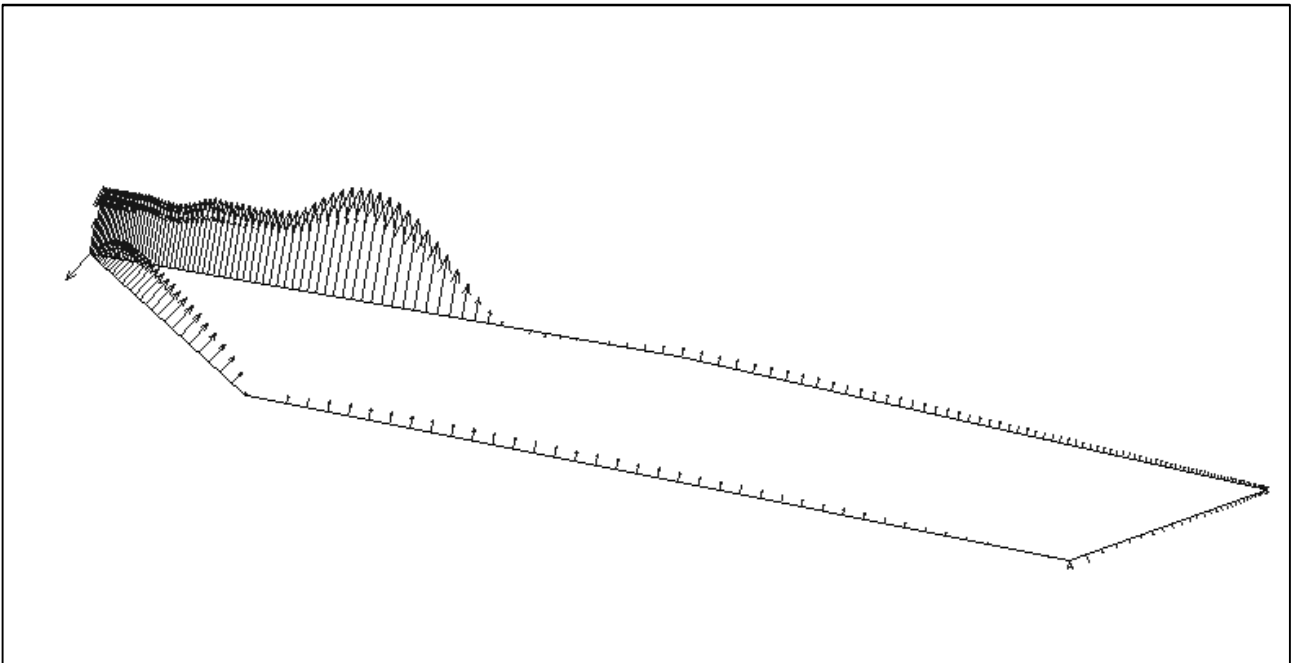
Figure 10(d). Forth Road Bridge deck (Configuration I): surface pressures at T2
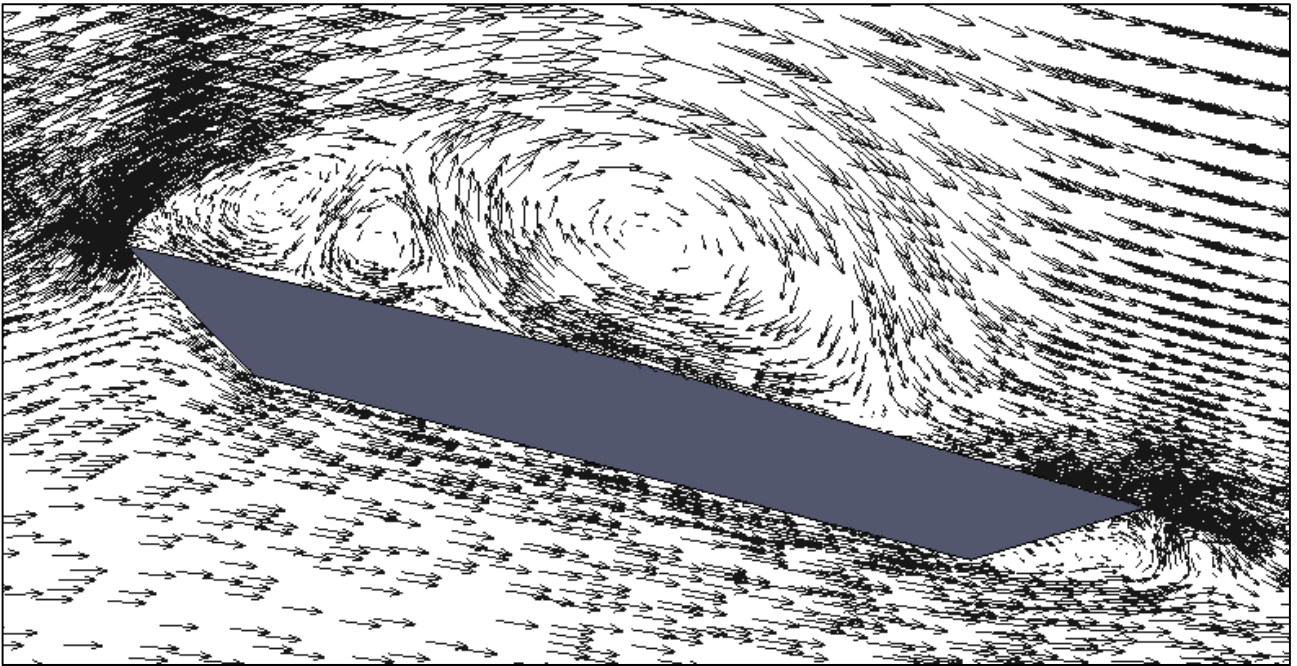
Figure 10(e). Forth Road Bridge deck (Configuration I): velocity fields of the fluid at T3
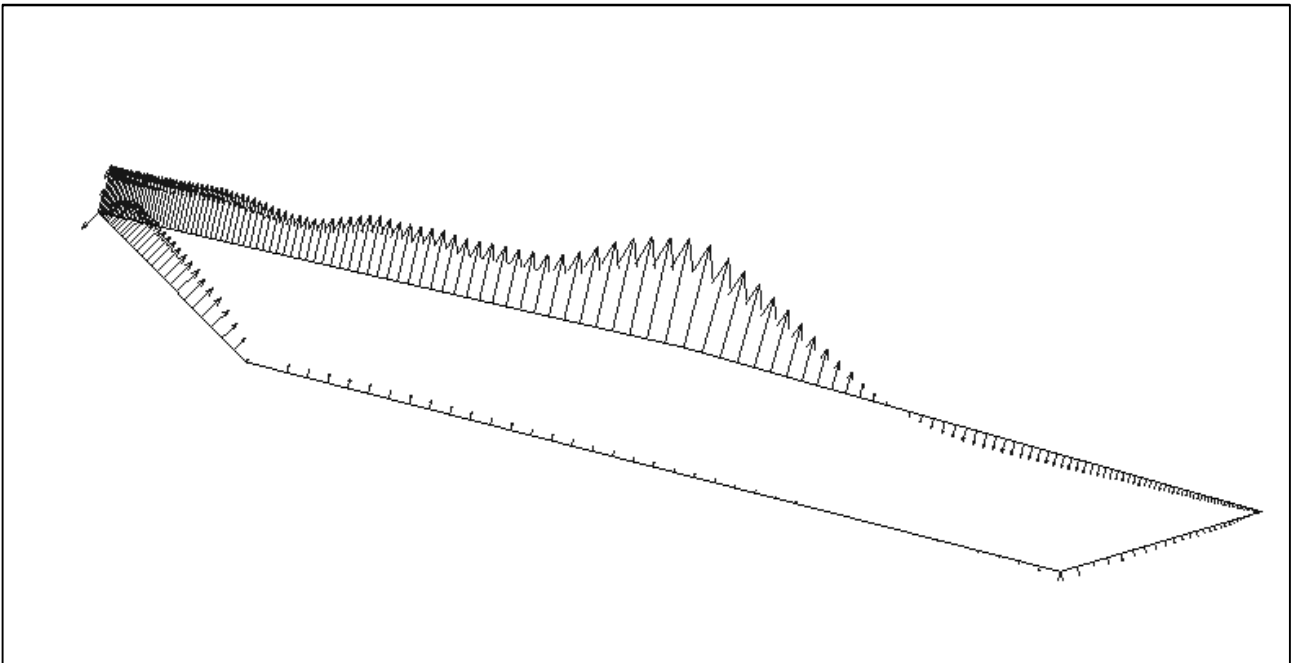
Figure 10(f). Forth Road Bridge deck (Configuration I): surface pressures at T3
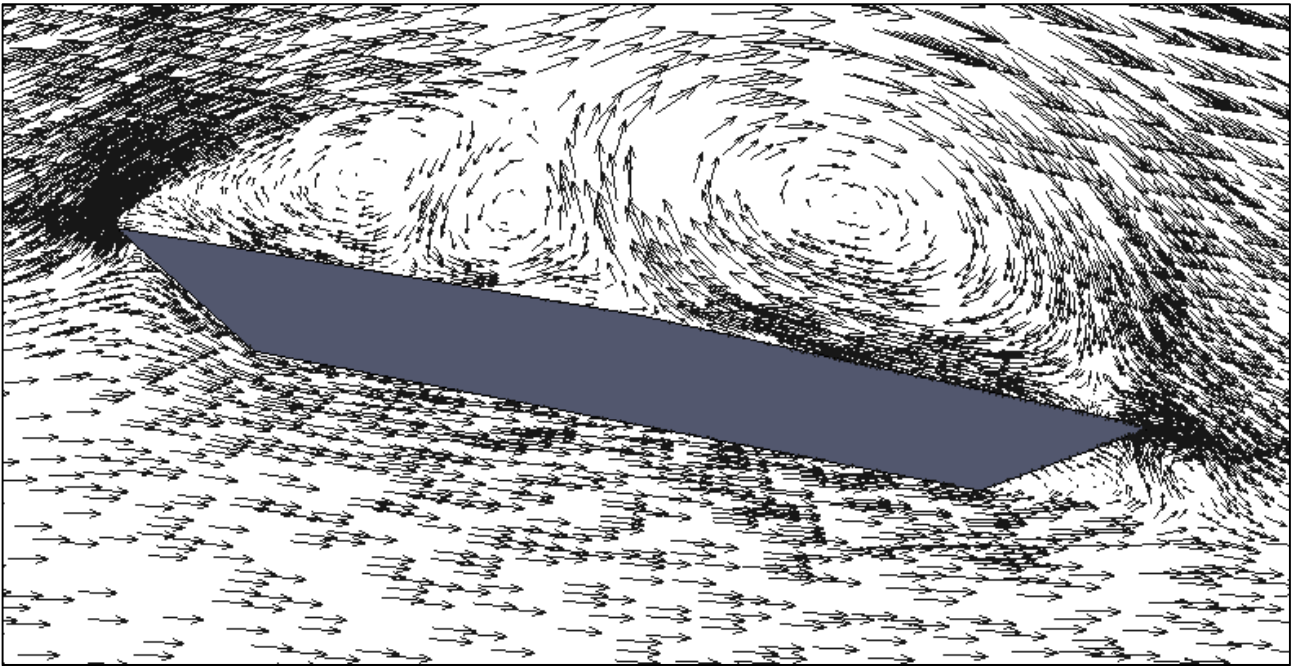
Figure 10(g). Forth Road Bridge deck (Configuration I): velocity fields of the fluid at T4

Figure 10(h). Forth Road Bridge deck (Configuration I): surface pressures at T4

Chapter 6

Aeroelastic optimisation study of the Forth Road Bridge deck

In this section, the presented simulation model is utilised to analyse the full fluid-structure interaction of the Forth Road Bridge deck in a configuration modified by the introduction of a couple of sloping barriers at the windward and leeward bridge deck edges. In Fig. 11 the geometric characteristics of the Forth Road Bridge deck in the modified configuration are shown. The wind barriers are 2.0 m high and inclined by 45 degrees with respect to the vertical direction. The fluid-structure interaction for the modified configuration is simulated by means of a block-structured grid made up of 39552 cells.

With the purpose of characterising the flutter type of the modified configuration, the angle Ψ defined as the phase-lag of the heaving response to the torsional response of the structure is used. In the case under examination, this angle is around $\Psi = -29°$. It is thus concluded that, in this case, the Forth Road Bridge deck is prone to a TB coupled flutter in which the torsional fundamental mode still dominates but to which the heaving fundamental mode contributes to a greater extent than in the case related to the bridge deck in the current configuration.

As it can be deduced from Fig. 12, the critical flutter wind velocity value is $U* = 82.0$

m/s (U_θ* = 6.58), which is higher than the one identified for the deck in its current configuration. Therefore this modification is to be considered effective in the improvement of the aero-elastic stability of the deck. Moreover, as observed with regard to the current configuration it is found that, for wind velocity values equal or greater than the critical flutter wind velocity value, the frequencies of the rotational and vertical wind-induced motion synchronise on a common frequency.

Figs. 13(a), 13(c), 13(e), 13(g) show the fluid velocity field which form around the deck in four time instants T1-T4 included in ½ of an oscillation cycle when flutter oscillations have been already developed. Figs. 13(b), 13(d), 13(f), 13(h) show the distribution of the surface normal unit-area forces exerted by the fluid on the deck (aerodynamic forces) in the same time instants.

- In Fig. 13(a) the velocity field in the first of the four considered instants is shown. In this instant a downward translation and a clockwise rotation of the deck is ongoing. The angle between the velocity vector that develop between the outer edge of the barrier placed on the left side of the deck (leading edge) and the direction identified by the barrier itself is not as high as to cause the flow detachment near the above-mentioned leading edge. Differently from that observed in the current configuration (I), a vortex does not form at the leading edge. Due to the abrupt change in direction of the velocity vector, the formation of a small vortical structure is observed in proximity to junction between the barrier and the deck. In Fig. 13(b)

the distribution of the components normal to the deck surface of the forces per unit area exerted by the fluid on the structure is shown. The higher values of the above-mentioned normal components are placed in proximity to the small vortical formation. The resultant of the components normal to the upper surface of the forces acting on the structure is directed in opposition to the downward translational motion of the deck. In this instant, the above-mentioned resultant acts in opposition to the downward displacement of the gravity centre and, therefore, provides a damping effect on the translational vertical motion of the deck. The point of application of the resultant is placed near the centre of the vortex, in an extremely far position from the centre of rotation of the deck. This resultant gives rise to a clockwise twisting moment. If, in this instant, the only elastic moment acted, the structure would rotate in an anti-clockwise direction. On the other hand, the above-mentioned clockwise twisting moment acts on the structure. This twisting moment prevails on the elastic moment and, consequently, is destined to amplify the clockwise rotation of the deck.

- By examining Fig. 13(c) it can be seen that, compared to the previous instant, there has been a growth of the dimensions of the vortical formation. By observing Fig. 13(d) it can be seen that an overall increase of the components normal to the upper surface of the forces acting on the structure is associated to the growth of the vortex. Differently from that observed in the current configuration (I), the vortex (in configuration II) does not drift along the upper deck surface. Consequently, the point of application of the resultant, placed near the

centre of the vortex, remains very far from the centre of rotation of the deck. The clockwise

twisting moment due to this resultant grows but, since the intensity of the above-mentioned

resultant is moderate, it reduces the contribution to the amplification of the clockwise rotation

of the deck. As well as in the previous instant, the resultant of the components normal to the

deck surface of the forces per unit area exerted by the fluid on the structure acts in opposition

to the downward translational motion of the gravity centre and, therefore, still provides a

damping effect on the motion itself.

- In the third of the four considered instants, the inversion of the translational and

the rotational motion of the deck has already taken place. In Fig. 13(e) a growth of the

dimensions of the vortical formation is observed. By examining Fig. 13(f) it can be seen that

an overall increase of the components normal to the upper surface of the forces acting on the

structure is associated to the growth of the vortex. Consequently, the intensity of the resultant

of these normal components increases. The vortex remains in the zone immediately downline

the point of junction between the barrier and the deck, so that the point of application of the

resultant, placed near the centre of the vortex, remains in an extremely far position from the

centre of rotation of the deck. In this instant the clockwise twisting moment, due to the

components normal to the upper surface of the forces acting on the structure, and the inertial

torque are opposite in sign to the elastic moment, which is dominant and acts in the same

direction as that of the rotation. In this instant, the resultant of the components normal to the

deck surface of the forces per unit area exerted by the fluid on the structure acts in the same direction as the upward displacement of the gravity centre. Consequently, in such instant the above-mentioned resultant provides a contribution in the amplification of the upward translational motion of the deck.

- In Fig. 13(g) it can be seen the gradual disappearing of the previously formed vortex. By examining Fig. 13(h) it is deduced that an overall increase of the components normal to the upper surface of the forces acting on the structure is associated to the dissolvement of the vortex. The elastic moment still acts in the same direction as that of the rotation. As well as in the previous instant, the resultant of the components normal to the deck surface of the forces per unit area exerted by the fluid on the structure acts in the same direction as the upward displacement of the gravity centre. Consequently, even in this instant the above-mentioned resultant provides a contribution in the amplification of the upward translational motion of the deck.

From the examination of Figs. 13(a), 13(c), 13(e), 13(g) and 13(b), 13(d), 13(f), 13(h) it is deduced that the presence of the sloped wind barriers produces a modification, compared to the current configuration (I), of the dynamics of vortices developed in the fluid-structure interaction. In configuration I, the angle between the velocity vector that develops in close vicinity to the leading edge and the direction identified by the line indicating the upper deck surface is sufficiently high to cause the flow detachment near the above-mentioned leading

edge. Immediately downline this detachment zone a large vortical structure forms, which drifts along the upper deck surface. The resultant of the components normal to the upper surface of the forces acting on the structure, whose point of application is placed near the vortex, moves along the upper deck surface. The twisting moment generated by the above-mentioned resultant changes in sign (from clockwise to anti-clockwise) during the ½ cycle of structural oscillations (as previously defined). Consequently (in configuration I) during the whole ½ cycle of structural oscillations the sign of the twisting moment is always coherent with the sign of rotation, and there is a continuous supply of energy from the fluid dynamic field to the structure that constitutes the reason for the instability of the torsional motion. The net effect of the resultant on the translational motion of the deck is to amplify the above-mentioned motion and provide a destabilising contribution.

In configuration II, the angle between the velocity vector that develops between the leading edge and the direction identified by the barrier itself is not as high as to cause the flow detachment near the above-mentioned leading edge. A small vortical structure is formed near the point of junction between the barrier and the deck. This vortical structure does not drift along the upper deck surface, but remains immediately downline the above-mentioned junction point. The components normal to the upper surface of the forces acting on the structure, whose point of application is placed near the vortex, does not drift along the upper deck surface, remaining always in an extremely far position from the centre of rotation of the

deck. The twisting moment generated by the above-mentioned resultant does not change in sign: this twisting moment acts in a clockwise direction during the whole ½ cycle of structural oscillations (as previously defined). Consequently, there is a phase of the ½ cycle of oscillations (the second) when the sign of the twisting moment generated by the above-mentioned resultant is not coherent with the sign of rotation, and creates a contrast and damping effect of the rotational motion itself. It is thus concluded that the aerodynamic modification can be considered effective in the mitigation of the amplitudes of the vibration which develop during the evolution of the flutter instability.
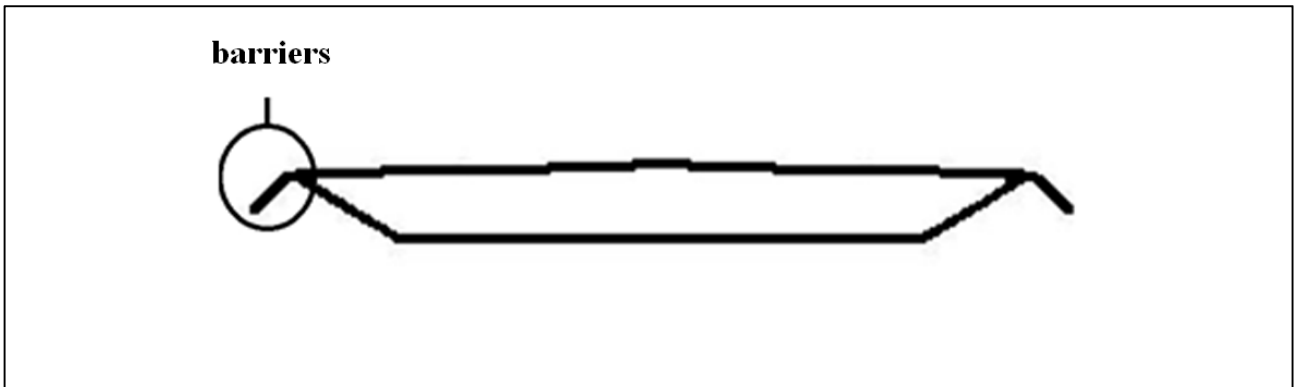
Figure 11. Forth Road Bridge deck cross-section configuration modified through a couple of sloping

barriers (Configuration II)
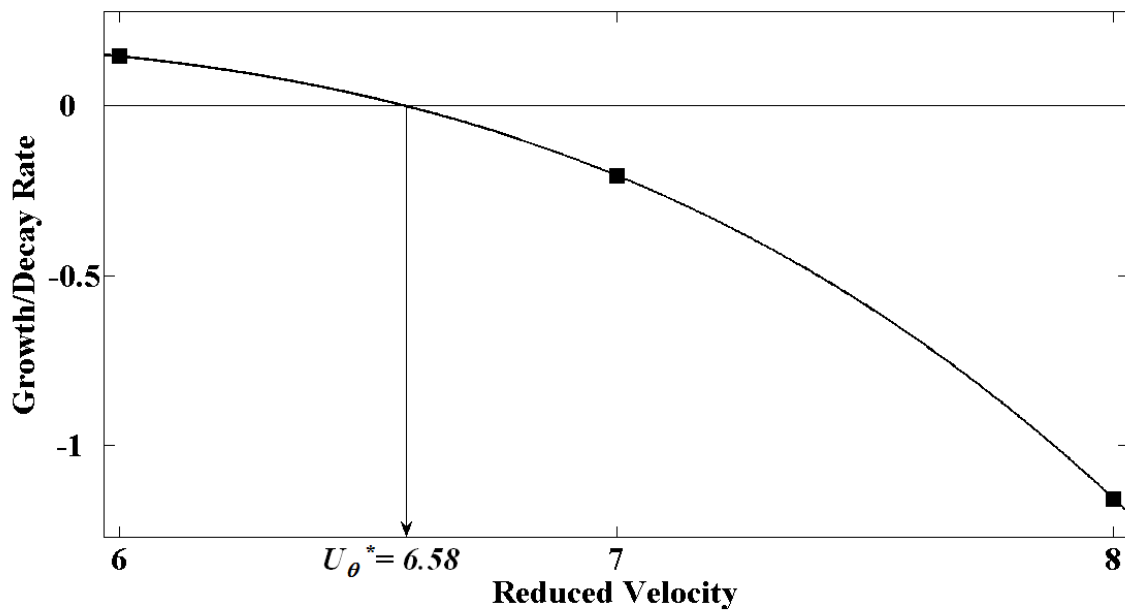
Figure 12. Growth/decay rate of the rotations of Forth Road Bridge deck vs reduced
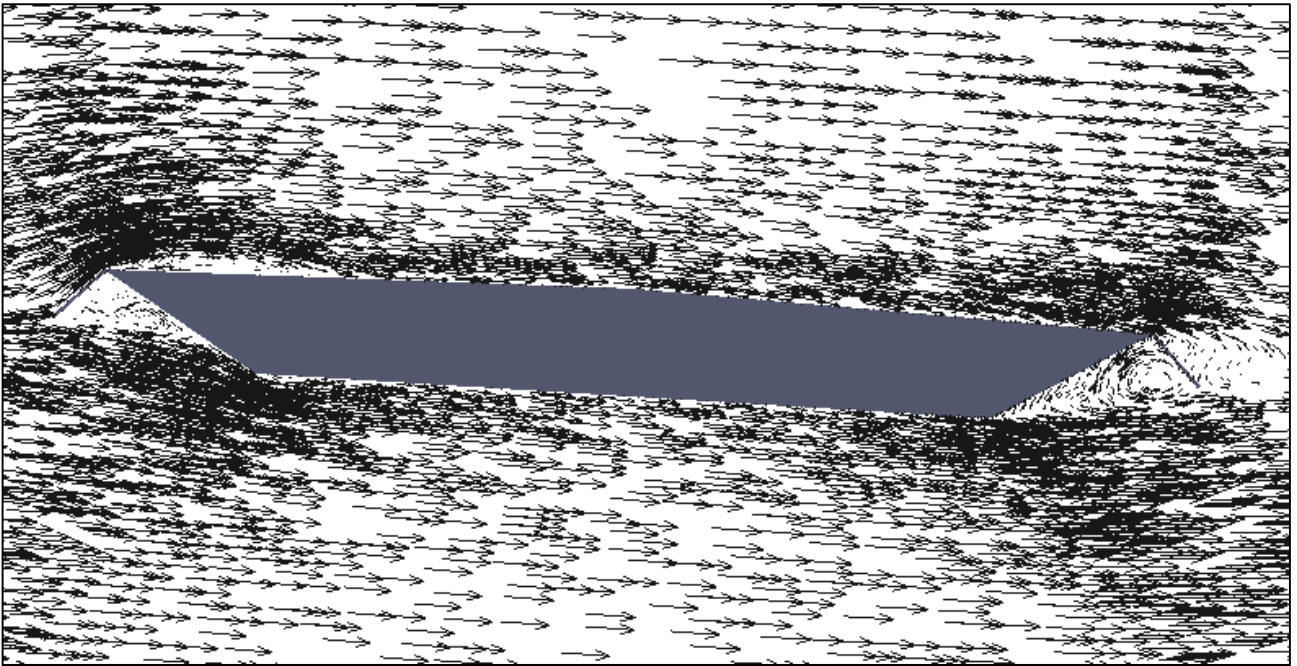
velocity (Configuration II)

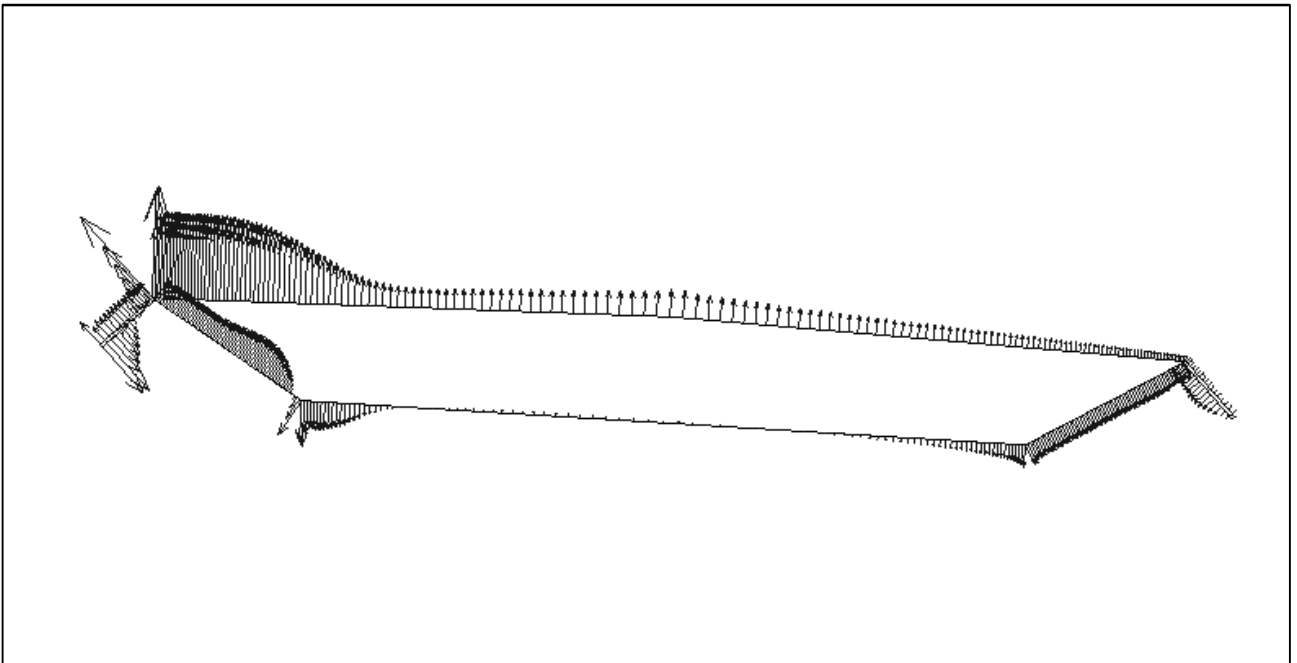Figure 13(a). Forth Road Bridge deck (Configuration II): velocity fields of the fluid at T1

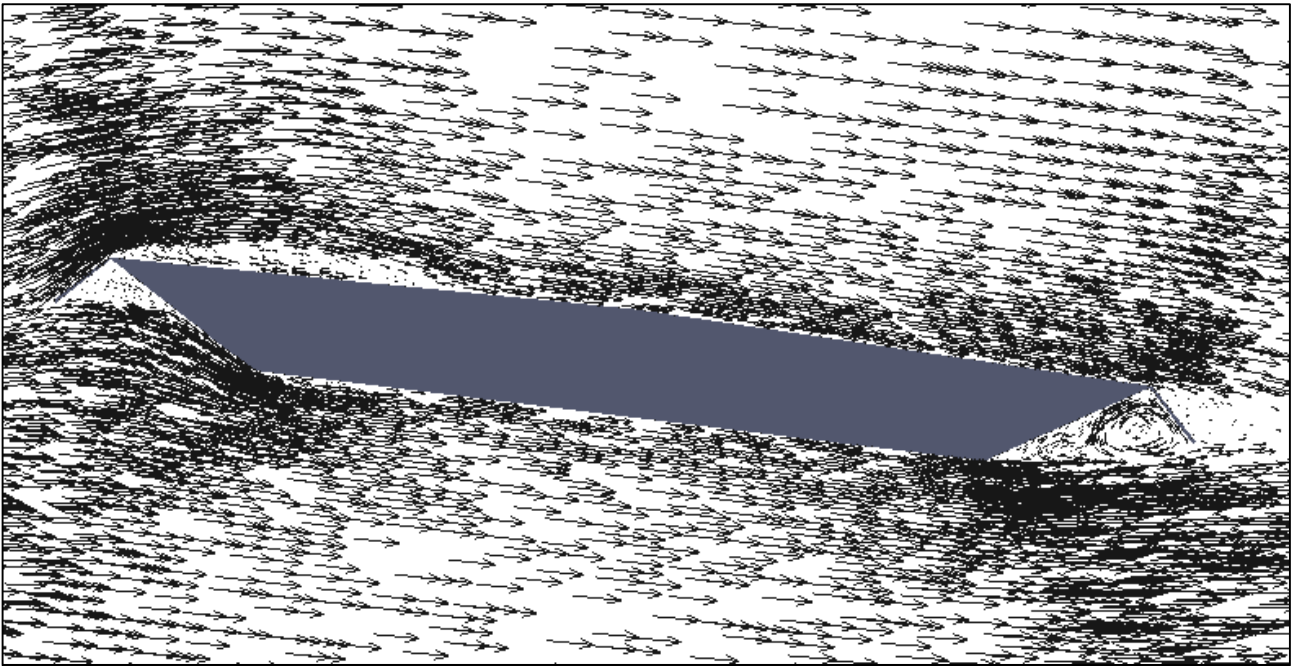Figure 13(b). Forth Road Bridge deck (Configuration II): surface pressures at T1

Figure 13(c). Forth Road Bridge deck (Configuration II): velocity fields of the fluid at T2
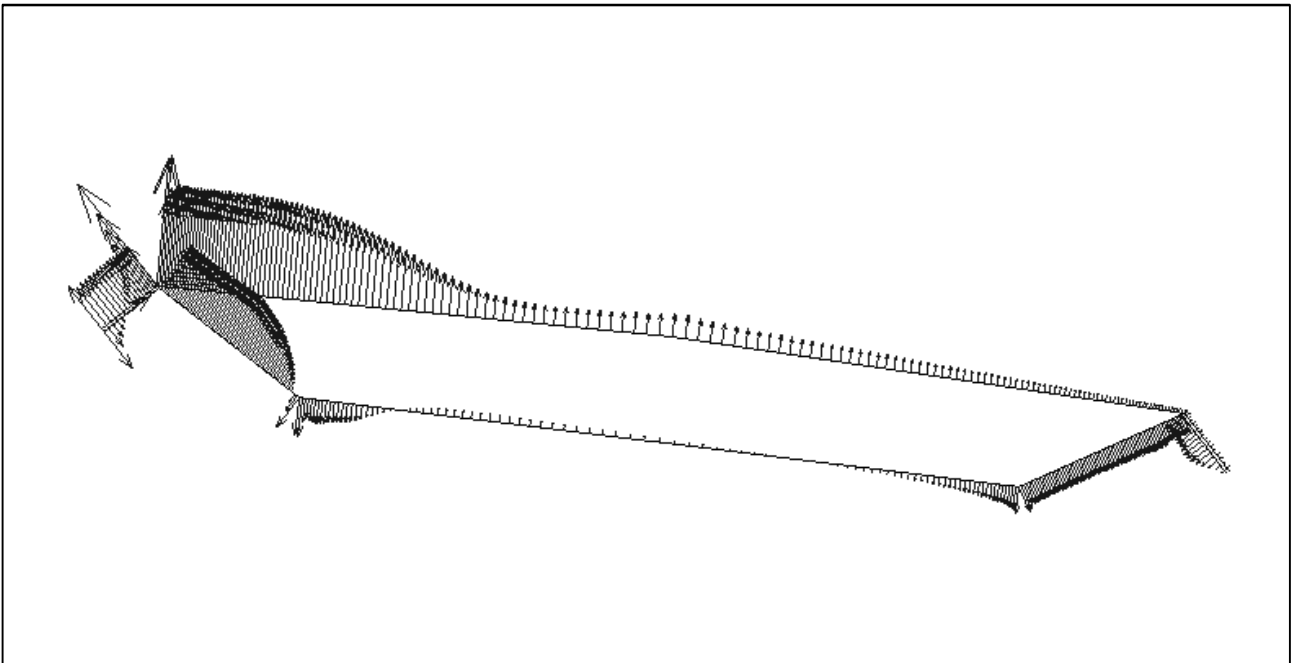

Figure 13(d). Forth Road Bridge deck (Configuration II): surface pressures at T2
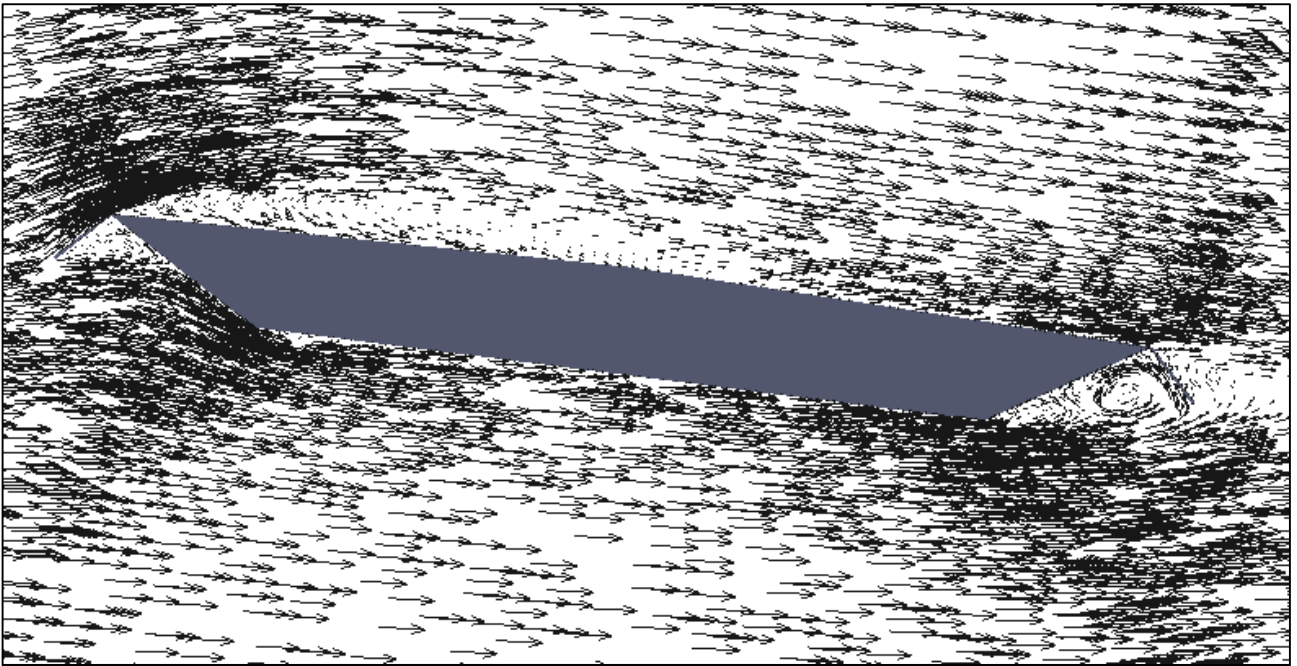
Figure 13(e). Forth Road Bridge deck (Configuration II): velocity fields of the fluid at T3
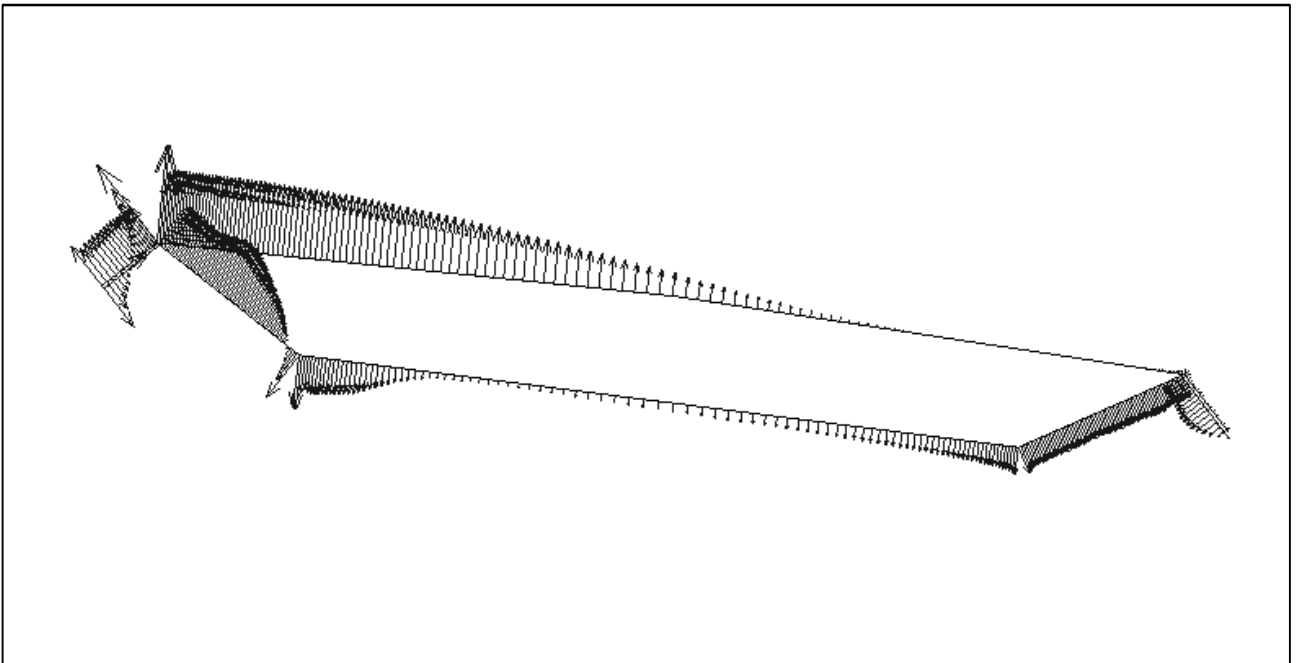

Figure 13(f). Forth Road Bridge deck (Configuration II): surface pressures at T3
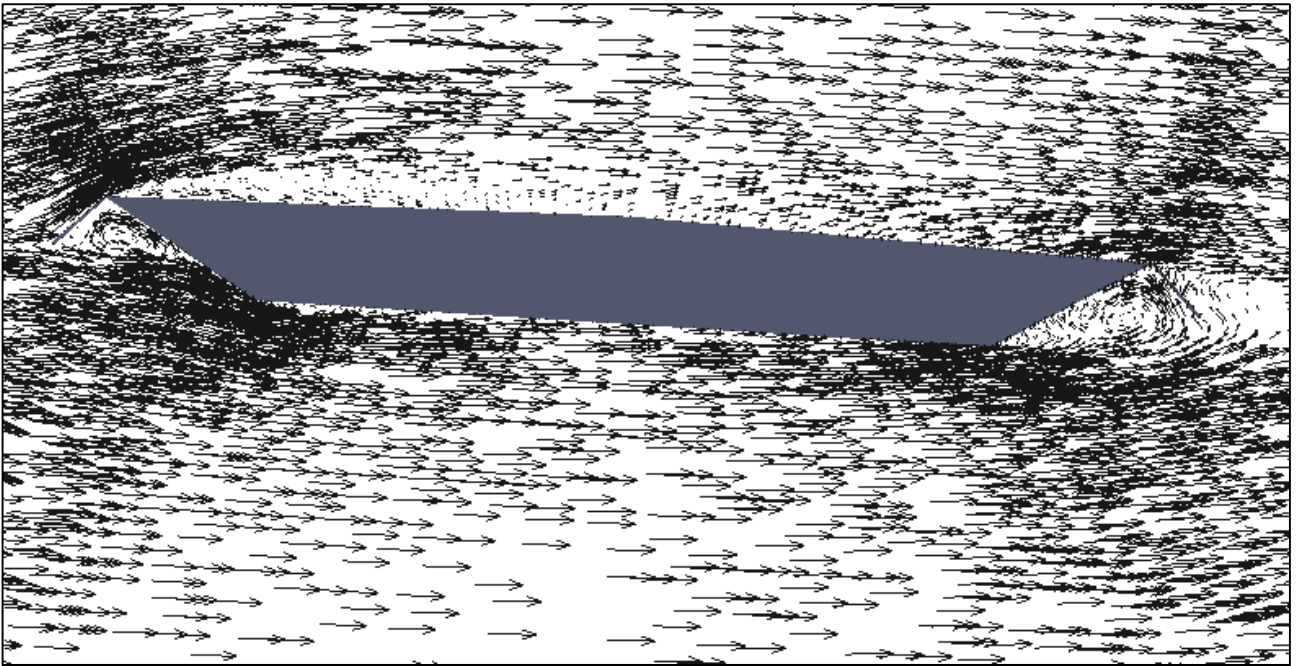
Figure 13(g). Forth Road Bridge deck (Configuration II): velocity fields of the fluid at T4
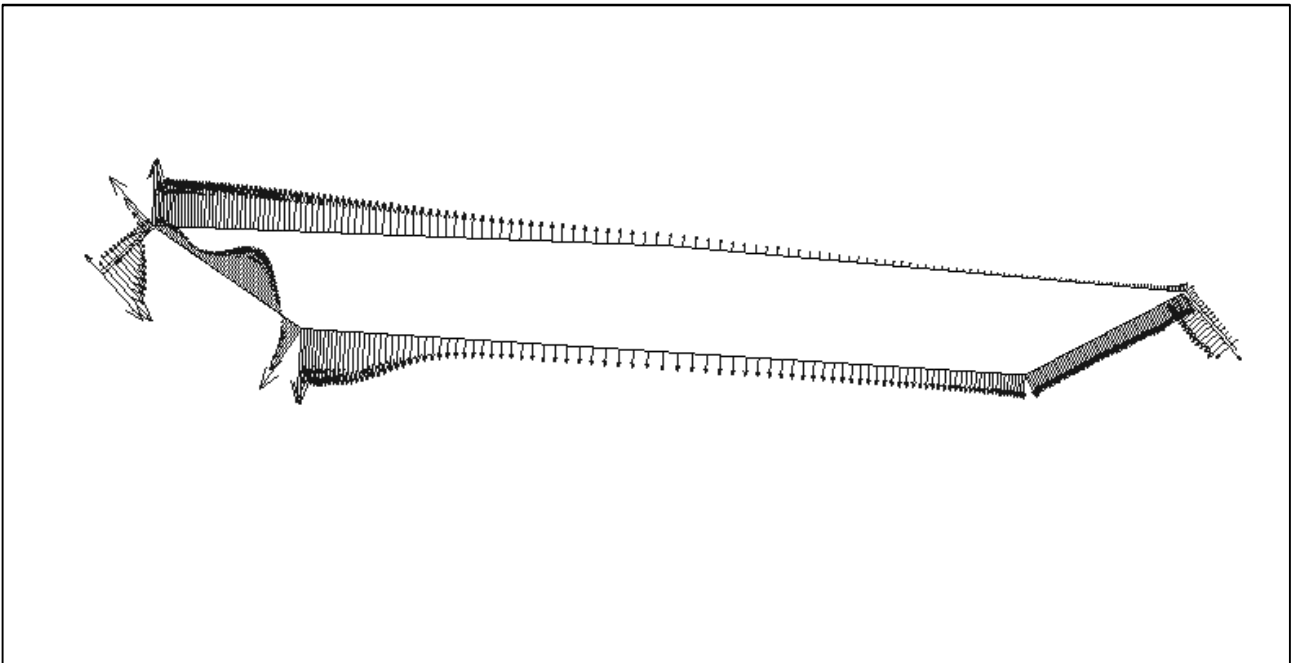

Figure 13(h). Forth Road Bridge deck (Configuration II): surface pressures at T4

<u>Conclusions</u>

In this thesis, a new method has been proposed for the investigation of aeroelastic phenomena for long-span bridges: the aerodynamic fields and the motion of structure are simulated simultaneously and in a coupled manner. The structure is represented as a bidimensional elastically suspended rigid body with two degrees of freedom whose natural frequencies correspond to those of the fundamental flexural and torsional modes of vibration of the structure. The aerodynamic fields are simulated by numerically integrating the Unsteady Reynolds-Averaged Navier-Stokes (URANS) equations with a finite volume scheme on moving grids which adapt to the structural motion. The URANS equations are completed by the turbulent closure relations which are expressed as a function of the turbulent kinetic energy, the turbulence frequency and the strain tensor according to the k-ω SST approach.

The model has been validated by comparing the numerical results with the experimental ones related to a slender body with rectangular cross-section and the Forth-Road Bridge deck. The model validation has been performed both in static conditions (i.e. under the assumption that all the degrees of freedom of the body are restrained) and dynamic conditions (i.e. under the assumption that the body is free to oscillate in the bending degree of freedom and in the torsional degree of freedom). In the static case, the Strouhal number, the lift and drag

coefficients have been taken as benchmark parameters by comparing the numerical results with those obtained experimentally with regard to the case study of a slender body with rectangular cross-section. In the dynamic case, the comparison has been performed in terms of critical flutter wind velocity by comparing the numerical results with those obtained experimentally with regard to the case study of the Forth Road Bridge deck.

The motion of the cross-section of the deck can be regarded as the superimposition of a rotational motion around the leading edge and a translational vertical motion of small entity. The torsional branch (TB) coupled flutter is defined as a coupled (torsional-flexural) flutter instability dominated by the fundamental torsional mode. It is demonstrated that in its current configuration the Forth Road Bridge deck is prone to a TB coupled flutter in which the torsional fundamental mode clearly dominates the heaving fundamental mode.

For wind velocities equal or greater than the critical wind flutter velocity, the deck starts to oscillate increasingly. Based on the analysis of the aerodynamic fields and the structural motion during the first cycles of oscillations of the deck (when the structure still exhibits oscillations of small amplitudes), it has been deduced that the reason for the onset of the instability lies in the fact that there are some portions of the cycle (within each of the first oscillation cycles) in which the aerodynamic field provides both the translational and the rotational motion with a higher supply of energy than that subtracted from the deck motion in the rest of the cycle.

Once the two-degree-of-freedom instability has been triggered, a progressive increase of the maximum amplitudes of the rotation angle takes place. Once a threshold value of the above angle is exceeded the recirculation bubble (which pulsates in proximity of the leading edge during the onset phase) starts to drift along the deck surface.

It has been shown that the reason for the amplification of the instability lies in the formation and the drift of large vortical formations along the deck surface. From the simulation of the phenomenon it emerges that, during the whole ½ cycle of structural oscillations, the sign of the twisting moment (generated by the resultant of the components normal to the upper surface of the forces acting on the structure) is always coherent with the sign of rotation. Consequently, there is a continuous supply of energy from the fluid dynamic field to the structure, that constitutes the reason for the amplification of the instability of the torsional motion. The result of the integral of the work, defined as the product between the resultant and the infinitesimal displacement of the gravity centre of the deck, over the whole cycle of structural oscillation is positive. Consequently, the net effect of the resultant on the translational motion of the deck is to amplify the above-mentioned motion and provide a destabilising contribution.

The numerical model has been also used to test the effect, on the aeroelastic stability of the Forth Road Bridge deck, of the introduction of a couple of sloping barriers at the windward and leeward bridge deck edges. It has been demonstrated that the aerodynamic

modifications, produced by the introduction of such barriers, is effective in increasing the critical flutter velocity and mitigating the vibration amplitudes which develop during the flutter instability.

References

Aris, R.:Vectors, tensors, and the basic equations of fluid mechanics. New York, NY, USA: Dover (1989).

Astiz, M. A., 1998. Flutter stability of very long suspension bridges. J. Bridge Eng. 3(3), 132-139.

Bosch, G., Rodi, W., 1998. Simulation of vortex shedding past a square cylinder with different turbulence models. Int. J. Numer. Met. Fluids 28, 601-616.

Braun, A. L., Awruch, A. M., 2008. Finite element simulation of the wind action over bridge sectional models: Application to the Guamà River Bridge (Parà State, Brazil). Finite elem. Anal. Des. 44, 105-122.

Bruno, L., Khris, S., 2003. The validity of 2D numerical simulations of vortical structures around a bridge deck. Math. Comput. Model 37, 795–828.

Brusiani, F., de Miranda, S., Patruno, L., Ubertini, F., Vaona, P., 2013. On the evaluation of bridge deck flutter derivatives using RANS turbulence models. J. Wind Eng. Ind. Aerod 119, 39–47.

Dowell, E., 2014. A Modern Course in Aeroelasticity: Fifth Revised and Enlarged Edition. Springer.

Ferziger, J, Peric, M. Computational methods for fluid mechanics. Springer Science and Business Media (2012).

Frandsen, J.B., 2004. Numerical brigde deck studies using finite elements. Part I: flutter. J. Fluids Struct 19, 171–191.

Gallerano, F, Napoli, E., 1999. A dynamic subgrid-scale tensorial eddy viscosity model. Continuum Mech. Thermodyn. 11(1), 1-14.

Gallerano, F., Cannata, G., 2011. Compatibility between reservoir sediment flushing and river protection. J. Hydraul Eng-ASCE 137 (10), 1111-1125.

Hertel, C., Schumichen, M., Lobig, S., Frohlich, J., Lang, J., 2013. Adaptive large eddy simulation with moving grids. Theor. Comp. Fluid Dyn. 27, 817-841.

Hines, J., Thompson, G. P., Lien, F. S., 2009. A turbulent flow over a square cylinder with prescribed and autonomous motions. Eng. Appl. Comp. Fluid 3(4), 573-586.

Jasak, H, Weller, H.G, Gosman, A.D. High resolution NVD differencing scheme for arbitrarily unstructured meshes. Int. J. Numer. Meth. Fluids 31(2), 431-449.

Jasak, H. Error analysis and estimation for finite volume method with applications to fluid flows. PhD thesis, Imperial College, University of London, 1996.

Katsuchi, H., Jones, N.P., Scanlan, R.H., 1999. Multimode coupled flutter and buffeting analysis of the Akashi-Kaikyo bridge. J.Struct. Eng 125, 60-70.

Larsen, A., 2000. Aerodynamics of the Tacoma Narrows Bridge – 60 Years Later. Structural Engineering International 4, 243-248.

Larsen, A., Walther, J.H., 1998. Discrete vortex simulation of flow around five generic bridge deck sections. J. Wind Eng. Ind. Aerod 77-78, 591–602.

Liu, X., Chen, Z., Liu. Z., 2012. Direct simulation method for flutter stability of bridge deck, in: Proceedings of the 7th International Colloquium on Bluff Body Aerodynamics and Applications (BBAA7), Shangai, China.

Mannini, C., Soda, A., Schewe, G., 2010. Unsteady RANS modelling of flow past a rectangular cylinder: Investigation of Reynolds number effects. Comput. Fluids 39, 1609-1624.

Mannini, C., Soda, A., Schewe, G., 2011. Numerical investigation on the three-dimensional unsteady flow past a 5:1 rectangular cylinder. J. Wind Eng. Ind. Aerod 99, 469–482.

Mannini, C., Soda, A., Voß, R., Schewe, G., 2010b. Unsteady RANS simulation of flow around a bridge section. J. Wind Eng. Ind. Aerod 98, 742–753.

Mannini, C., Marra, A.M., Bartoli, G., 2014. VIV–galloping instability of rectangular cylinders: Review and new experiments. J. Wind Eng. Ind. Aerod 132, 109-124.

Matsumoto, M., Matsumiya, H., Fujiwara, S., Ito, Y., 2010. New consideration on flutter properties based on step-by-step analysis. J. Wind Eng. Ind. Aerod 98 (12), 429-437.

Mendes, P.A., Branco, F.A., 1998. Numerical wind studies for the Vasco da Gama Bridge, Portugal. Struct. Eng. Int 8 (2), 124–128.

Menter, F., Carregal Ferreira, J., Esch, T., Konno, B., 2003. The SST Turbulence Model with Improved Wall Treatment for Heat Transfer Predictions in Gas turbines, in: Proceedings of the International Gas Turbine Congress, Tokyo, Japan.

Menter, F. R., 2009. Review of the shear-stress transport turbulence model experience from an industrial perspective. Int. J. Comput. Fluid D. 23, 305-316.

Morgenthal, G., McRobie, A., 2002. A comparative study of numerical methods for fluid-structure interaction analysis in long-span bridge design. Wind Struct 5 (2-4), 101–114.

Nieto, F., Owen, J. S., Hargreaves, D. M., Hernandez, S., 2014. Bridge deck flutter derivatives: Efficient numerical evaluation exploiting their independence. J. Wind Eng. Ind. Aerod 136, 138-150.

Norris, S.E. A parallel Navier-Stokes solver for natural convection and free-surface flow. 2000.

Oka, S., Ishihara, T., 2009. Numerical study of aerodynamic characteristics of a square prism in a uniform flow. J. Wind Eng. Ind. Aerod 97, 548-559.

Rhie, C. M., Chow, W. L., 1983. Numerical study of the turbulent flow past an airfoil with trailing edge separation. AAIA Journal 21 (11), 1525-1532.

Robertson, I., Sherwin, S. J., Bearman, P. W., 2003. Flutter instability prediction techniques for bridge deck sections. Int. J. Numer. Meth. Fluids 43, 1239-1256.

Rossmanith, J. A., Bale, D. S., LeVeque, R. J., 2004. A wave propagation algorithm for hyperbolic systems on curved manifolds. J Comput. Phys. 199(2), 631-662.

Sarwar, M.W., Ishihara, T., 2010. Numerical study on suppression of vortex-induced vibrations of box girder bridge section by aerodynamic countermeasures. J. Wind Eng. Ind. Aerod 98, 701-711.

Sarwar, M.W., Ishihara, T., Shimada, K., Yamasaki, Y., Ikeda, T., 2008. Prediction of aerodynamic characteristics of a box girder bridge section using the LES turbulence model. J. Wind Eng. Ind. Aerod 96, 1895–1911.

Schewe, G., 2006. Influence of the Reynolds-number on flow-induced vibrations of generic bridge sections, in: Proceedings of the International Conference on Bridges, Dubrovnik, Croatia.

Schewe, G., 2009. Reynolds-number effects in flow around a rectangular cylinder with aspect ratio 1:5, in: Proceedings of the Fifth European and African Conference on Wind Engineering, Florence, Italy.

Schewe, G., 2013. Reynolds-number-effects in flow around a rectangular cylinder with aspect ratio 1:5. J. Fluid Struct. 39, 15-26.

Shimada, K., Ishihara, T., 2011. Predictability of unsteady two-dimensional k-ε model on the aerodynamic instabilities of some rectangular prisms. J. Fluids Struct 28, 20–39.

Starossek, U., 1998. Complex notation in Flutter Analysis. J.Struct. Eng. 124(8), 975-977.

Taylor, I., Vezza, M., 2002. Aeroelastic stability analysis of a bridge deck with added vanes using a discrete vortex method. Wind Struct. 5, 277-290.

Uyttersprot, L., 2014. Inverse Distance Weighting Mesh Deformation. Master of Science Thesis, Delft University of Technology.

Vairo, G., 2003. A numerical model for wind loads simulation on long-span bridges. Simulat. Model. Pract. Theory 11, 315–351.